

AWARD NUMBER:

W81XWH-13-1-0391

TITLE:

MRI-Derived Cellularity Index as a Potential Noninvasive Imaging Biomarker of Prostate Cancer

PRINCIPAL INVESTIGATOR:

David S. Karow, MD, PhD

CONTRACTING ORGANIZATION:

University of California, San Diego
Nc'Lqmc.'EC"; 42; 5"

REPORT DATE:

October 2014

TYPE OF REPORT:

Annual Report

PREPARED FOR: U.S. Army Medical Research and Materiel Command
Fort Detrick, Maryland 21702-5012

DISTRIBUTION STATEMENT: Approved for Public Release;
Distribution Unlimited

The views, opinions and/or findings contained in this report are those of the author(s) and should not be construed as an official Department of the Army position, policy or decision unless so designated by other documentation.

REPORT DOCUMENTATION PAGE				Form Approved OMB No. 0704-0188	
Public reporting burden for this collection of information is estimated to average 1 hour per response, including the time for reviewing instructions, searching existing data sources, gathering and maintaining the data needed, and completing and reviewing this collection of information. Send comments regarding this burden estimate or any other aspect of this collection of information, including suggestions for reducing this burden to Department of Defense, Washington Headquarters Services, Directorate for Information Operations and Reports (0704-0188), 1215 Jefferson Davis Highway, Suite 1204, Arlington, VA 22202-4302. Respondents should be aware that notwithstanding any other provision of law, no person shall be subject to any penalty for failing to comply with a collection of information if it does not display a currently valid OMB control number. PLEASE DO NOT RETURN YOUR FORM TO THE ABOVE ADDRESS.					
1. REPORT DATE October 2014		2. REPORT TYPE Annual report		3. DATES COVERED 15 Sep 2013 - 14 Sep 2014	
4. TITLE AND SUBTITLE MRI-Derived Cellularity Index as a Potential Noninvasive Imaging Biomarker of Prostate Cancer				5a. CONTRACT NUMBER	
				5b. GRANT NUMBER W81XWH-13-1-0391	
				5c. PROGRAM ELEMENT NUMBER	
6. AUTHOR(S) David S. Karow, MD, PhD E-Mail: dkarow@ucsd.edu				5d. PROJECT NUMBER	
				5e. TASK NUMBER	
				5f. WORK UNIT NUMBER	
7. PERFORMING ORGANIZATION NAME(S) AND ADDRESS(ES) UNIVERSITY OF CA, SAN DIEGO LA JOLLA, CA 92093-0621				8. PERFORMING ORGANIZATION REPORT NUMBER	
9. SPONSORING / MONITORING AGENCY NAME(S) AND ADDRESS(ES) U.S. Army Medical Research and Materiel Command Fort Detrick, Maryland 21702-5012				10. SPONSOR/MONITOR'S ACRONYM(S)	
				11. SPONSOR/MONITOR'S REPORT NUMBER(S)	
12. DISTRIBUTION / AVAILABILITY STATEMENT Approved for Public Release; Distribution Unlimited					
13. SUPPLEMENTARY NOTES					
14. ABSTRACT Standard magnetic resonance imaging (MRI) of the prostate lacks sensitivity in the diagnosis and staging of prostate cancer (PCa). To improve the operating characteristics of prostate MRI in the detection and characterization of PCa, we developed a novel, enhanced MRI diffusion technique using restriction spectrum imaging (RSI-MRI). This technique leads to greater tumor conspicuity and also more accurate localization due to spatial distortion correction techniques. As of this annual report, we show that these techniques increase our ability to detect extraprostatic extension, improve accuracy of targeted biopsies and we show that our quantitative imaging signal (RSI z-score) correlates with Gleason grade on final histopathology.					
15. SUBJECT TERMS: nothing listed					
16. SECURITY CLASSIFICATION OF: Unclassified.			17. LIMITATION OF ABSTRACT Unclassified	18. NUMBER OF PAGES 69	19a. NAME OF RESPONSIBLE PERSON USAMRMC
a. REPORT Unclassified	b. ABSTRACT Unclassified	c. THIS PAGE Unclassified			19b. TELEPHONE NUMBER (include area code)

Table of Contents

	<u>Page</u>
1. Introduction.....	1
2. Keywords.....	1
3. Overall Project Summary.....	2
4. Key Research Accomplishments.....	3-5
5. Conclusion.....	6
6. Publications, Abstracts, and Presentations.....	6
7. Inventions, Patents and Licenses.....	6
8. Reportable Outcomes.....	6
9. Other Achievements.....	6
10. References.....	7
11. Appendices.....	7

Introduction:

Enhanced MRI imaging techniques called restriction spectrum imaging (RSI) has been utilized to identify glioblastoma multiforme (GBM) brain tumors (1). The output from these techniques has been termed the tumor 'RSI cellularity index' and provides significantly greater accuracy in distinguishing brain tumor from normal tissue than traditional imaging measures. The RSI tumor signal was noted to be 10-fold greater than conventional imaging measures (1-2). In addition, these imaging techniques are corrected for spatial distortions that allows for more accurate localization of the tumor signal (3). In prostate cancer, increasing Gleason score correlates with loss of normal gland formation, loss of peripheral gland tubular structure and increased cellularity. Therefore, we hypothesize that the RSI cellularity index will correlate with higher tumor grade based on Gleason score and will provide significantly greater accuracy in discriminating aggressive tumor from benign and indolent lesions when compared to current imaging techniques. Based on its prior ability to discriminate between brain tumors and adjacent normal tissue with high accuracy and high signal to noise, we hypothesize that the RSI cellularity index will perform similarly in prostate tissue. We propose a non-invasive (without endorectal coil or IV contrast), rapid imaging test based on these procedures. The goal of the current research is to test whether that objective is feasible.

Keywords:

DCE = dynamic contrast enhancement

DWI = diffusion weighted imaging

ADC = apparent diffusion coefficient

RSI = restriction spectrum imaging

CI = cellularity index

EPI = echo planar imaging

Prostate cancer screening

Prostate cancer staging

Non-invasive imaging

Overall Project Summary:

Specific Aim 1:

All aspects of Specific Aim 1 have been accomplished. Existing pulse sequences at UCSD have been modified for signal optimization in patients. Post-processing techniques for displaying and analyzing RSI data have been developed and optimized. The whole mount sectioning protocol for prostate specimens at UCSD has been optimized. Local IRB approval was obtained under HRPP#071983, which was also accepted by DoD.

Specific Aim 2:

Major Tasks 2 and 3 include data collection and analysis and is ongoing. MR imaging with an endorectal coil for 85 patients, without an endorectal coil for 10 patients, and TIFFs of whole-mount pathology slides for 28 patients, have been anonymously transferred to UCSD from UCLA for analysis. In parallel we have been collecting imaging and pathology data at UCSD without an endorectal coil using similar imaging and pathology techniques. All imaging evaluated from UCSD and UCLA have RSI techniques incorporated. As noted below we have imaged 182 patients at UCSD with 17 whole mount pathology sections. We have currently collected roughly 33% of our goal of 150 patients with whole mount pathology sections. Analysis of these data has so far resulted in one published manuscript (White et al, Cancer Research 2014), one accepted manuscript (Rakow-Penner, et al.) and one submitted manuscript (Liss et al.). In summary, all tasks and subtasks of Aim 2 have been partially performed. Completion will follow after all patients have been imaged over the next few months.

Specific Aim 3:

Major Task 4 and 5 includes data collection and analysis and is ongoing. Imaging using RSI has been implemented as part of the patient standard of care at UCSD, both for screening and for pre-operative MRI. All patients undergoing pre-operative MRI at UCSD are scanned using the modified imaging protocol without an endorectal coil, resulting in 182 scans at UCSD during the covered grant period. Prostate tissue is obtained from each prostatectomy patient and processed using the optimized whole mount sectioning protocol. Seventeen patients at UCSD underwent prostatectomy with subsequent whole-mount pathology during the covered grant period. We are continuing to collect imaging and pathology data. Our stated goal in the SOW was to collect imaging and whole mount path data from 75 patients by month 17. We expect to reach this goal as patients with imaging over the last year will be finally going to prostatectomy. We can expect to perform a similar analysis as in Aim 2 in this subset of patients that were imaged without an endorectal coil. In summary, all tasks and subtasks of Aim 3 have been partially performed. Completion will follow after all patients have been imaged over the next few months.

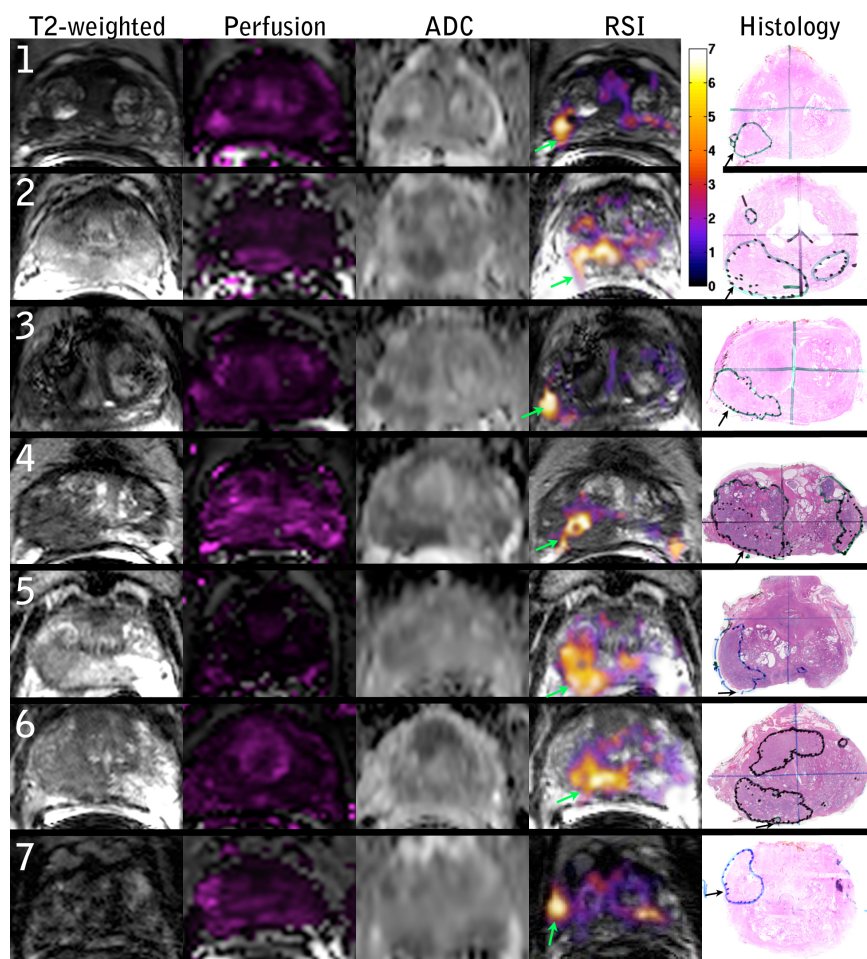
Key Research Accomplishments:

1) We have identified spatial distortion in conventional diffusion weighted imaging and, using RSI, we are able to correct for it. This table summarizes the results for 28 patients. The results show that distortions of tumor signal can be as great as 1.3 cm if left uncorrected.

Table 2. Distortion distance of the whole prostate and tumor regions of interest due to B0 inhomogeneity		
	Mean (standard deviation) (mm)	Maximum distortion (mm)
Whole prostate distortion	3.2 (2.2)	12
Tumor ROI distortion	3.2 (2.4)	13

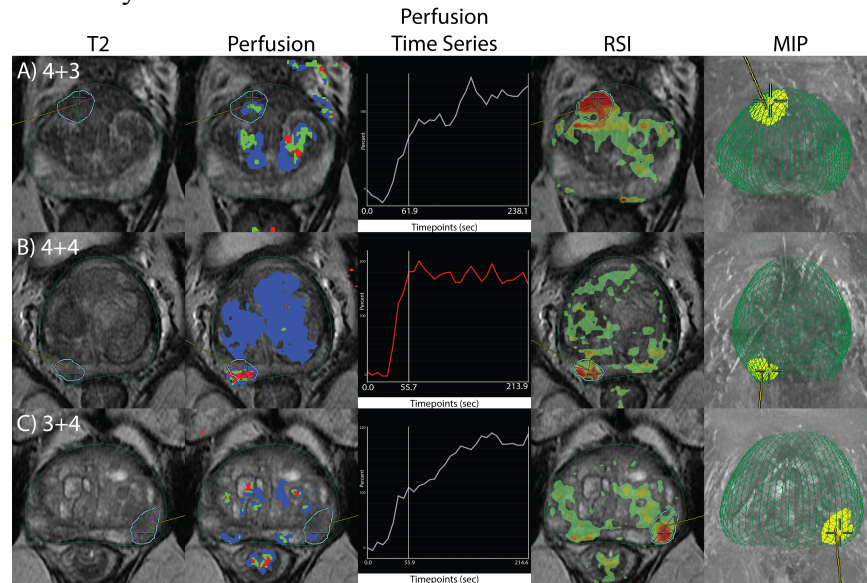
Rakow-Penner et al, in preparation

2) As a result of the correction for distortion, RSI has improved our detection of extra prostatic extension by more accurately localizing tumor location.



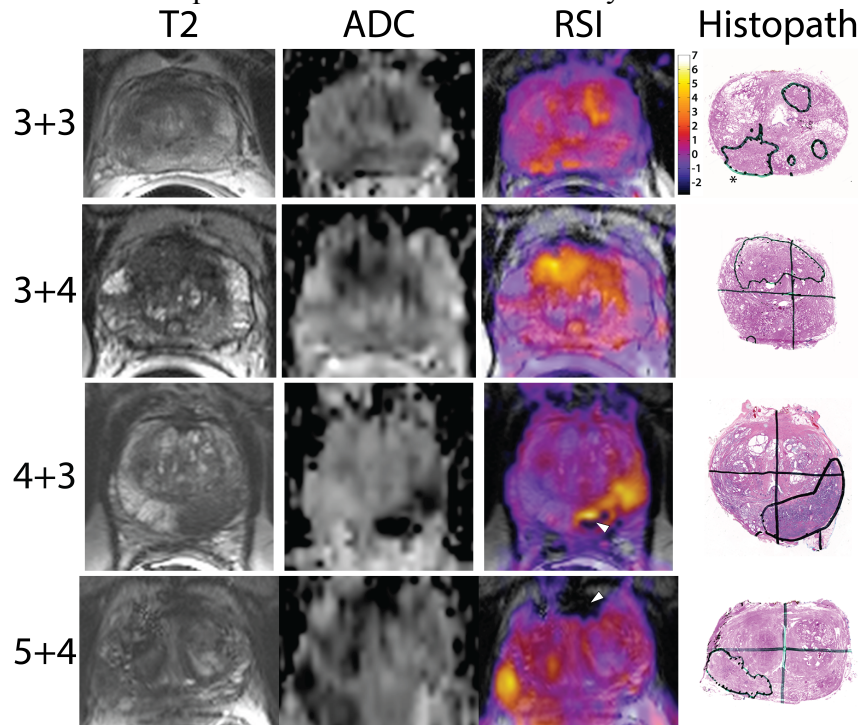
MR imaging and whole mount pathology for 7 prostate cancer patients. Column 1: T2 – weighted images, column 2: Perfusion K_{trans} maps, column 3: standard apparent diffusion coefficient (ADC) maps ($b = 0, 100, 400$, and 800 s/mm^2), column 4: RSI z-score maps, column 5: whole mount pathology with tumor and area of EPE identified. Color bar represents zscores from 0 to 7 for the RSI maps. (Rakow-Penner et al, accepted)

3) RSI imaging has also been implemented as part of the work flow for defining tumor regions of interest for targeted biopsy using Dynacad and UroNav MR-fused ultrasound targeted biopsy software. Due to increased conspicuity of the RSI signal compared to perfusion (DCE) and conventional DWI, as well as correction of spatial distortions, we are able to localize small tumors with accuracy as illustrated below. While this was not an Aim of the DoD proposal, this is certainly a noteworthy achievement.

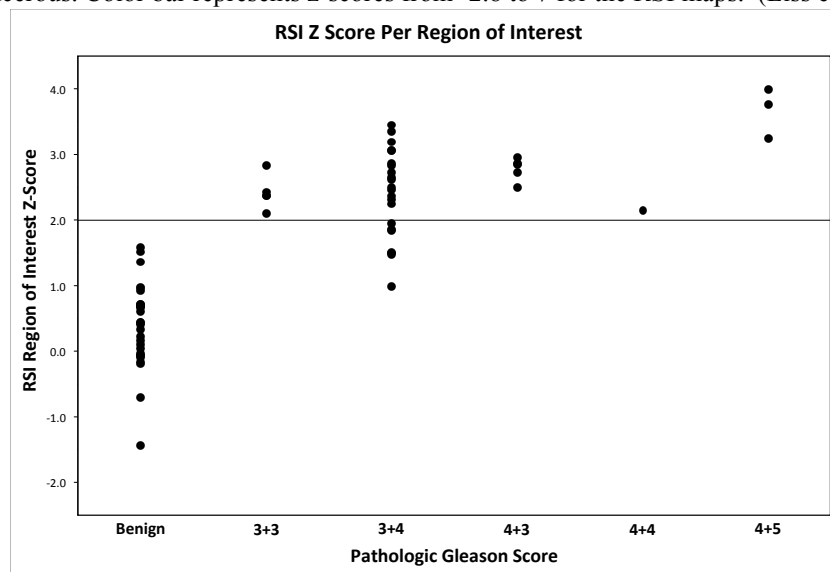


Images from three patients who underwent targeted biopsy. The first column demonstrates the T2 map with the ROI drawn to guide the MR-fused ultrasound guided biopsy. The second column displays the Dynacad perfusion maps, where red signifies rapid intense enhancement with washout, green signifies rapid intense enhancement with plateau washout and blue signifies gradual enhancement. The third column demonstrates the perfusion curves for the location identified by the crosshair in the other images. The fourth column illustrates a heatmap based on the RSI overlaid on T2 images, with red regions correlating to the areas of greatest restricted diffusion. The fifth column shows maximum intensity projections of the prostate boundary (green) and ROI for targeting (yellow). A) Patient with three negative previous biopsies. The targeted biopsy found Gleason 4+3 cancer. B) Patient with previous incomplete radiation therapy for response to low-grade cancer. Targeted biopsy found Gleason 4+4 cancer. C) Patient with previous biopsy demonstrating low-grade cancer. Targeted biopsy found Gleason 3+4 cancer.

4) Quantitatively, we have shown RSI to be at least as good as ADC in detecting high-grade cancer. Our results suggest that the RSI z-score may accurately predict Gleason grade. The RSI z-score is a quantitative measure of cellularity.



Representative images showing RSI z-score maps across Gleason scores. The y-axis shows the pathologic Gleason score with the x-axis designating the MRI sequence. The last column displays the whole mount pathology with the corresponding cancer region of interest circled in black. The star 3+3 pathologic figure represents the lesion with 3+3 prostate cancer while the other lesions are 4+3. White arrows in the 4+3 and 5+4 RSI indicate regions where the ADC is dark and would be suspicious for tumor, but the RSI reveals these are regions with signal void and are unlikely to be cancerous. Color bar represents z-scores from -2.8 to 7 for the RSI maps. (Liss et al, submitted)



RSI z-score value grouped by pathologic Gleason score for 28 patients: The y-axis represents the RSI z-score derived from a given region of interest. The x-axis demonstrates the pathological Gleason scores in increasing levels of aggressiveness from left to right. Each data point represents one region of interest corresponding to a location on the whole mount prostatectomy specimen contoured by a GU pathologist (Liss et al, submitted).

Conclusion:

- We have identified the distortions in RSI and conventional diffusion weighted imaging and corrected for them in our postprocessing stream. This has increased our ability to detect extraprostatic extension and helped to increase the accuracy of targeted biopsies.
- We have optimized and implemented a non-invasive imaging measure of Gleason grade (RSI z –score) that is at least as good as standard ADC.
- All RSI cases scanned at UCSD have been performed without an endorectal coil and with sequences of less than 10 minutes, suggesting the feasibility of using this protocol clinically on a non-invasive screening basis.

Publications, Abstracts and Presentations:

White, N.S., McDonald, C.R., Farid, N., Kuperman J., **Karow, D.**, Schenker-Ahmed, N.M., Bartsch, H., Rakow-Penner, R., Holland, D., Shabaik, A., Bjornerud, A., Hope, T., Hattangadi-Gluth, J., Liss, M., Parsons, J.K., Chen, C.C., Raman, S., Margolis, D., Reiter, R.E., Marks, L., Kesari, S., Mundt, A.J., Kane, C.J., Carter, B.S., Bradley, W.G., and Dale, A.M. Diffusion-Weighted Imaging in Cancer: Physical Foundations and Applications of Restriction Spectrum Imaging. *Cancer Research*. 74;4638, Sept. 2014.

Rakow-Penner, R.A., White, N.S., Parsons, J.K., Choi, H.W., Liss, M.A., Kuperman, J.M., Schenker-Ahmed, N., Bartsch, H., Mattrey, R.F., Bradley, W.G., Shabaik, A., Huang, J., Margolis, D.J., Raman, S.S., Marks, L., Kane, C.J., Reiter, R.E., ***Karow, D.S.** and Dale, A.M. Novel Technique for Characterizing Prostate Cancer Utilizing MRI Restriction Spectrum Imaging: Proof of Principle and Initial Clinical Experience with Extra-Prostatic Extension. *Prostate Cancer Prostatic Diseases*. *Accepted pending revisions*. ***Corresponding author**.

Liss, M.A., White, N.S., Parsons, J.K., Schenker-Ahmed, N., Rakow-Penner, R.A., Kuperman, J.M., Bartsch, H., Choi, H.W., Mattrey, R.F., Bradley, W.G., Shabaik, A., Huang, J., Margolis, D.J., Raman, S.S., Marks, L., Kane, C.J., Reiter, R.E., Dale, A.M., **Karow, D.S.** MRI-derived Restriction Spectrum Imaging Cellularity Index is Associated with High Grade Prostate Cancer on Radical Prostatectomy Specimens. *Submitted*.

Inventions, Patents and Licenses:

None

Reportable Outcomes:

None

Other Achievements:

None

References:

- (1) White, N. S., McDonald, C. R., Farid, N. et al.: Improved conspicuity and delineation of high-grade primary and metastatic brain tumors using "restriction spectrum imaging": quantitative comparison with high B-value DWI and ADC. *AJNR Am J Neuroradiol*, **34**: 958, 2013
- (2) White, N. S., Leergaard, T. B., D'Arceuil, H. et al.: Probing tissue microstructure with restriction spectrum imaging: Histological and theoretical validation. *Hum Brain Mapp*, **34**: 327, 2013
- (3) Holland, D., Kuperman, J. M., Dale, A. M.: Efficient correction of inhomogeneous static magnetic field-induced distortion in Echo Planar Imaging. *Neuroimage*, **50**: 175, 2010

Appendices:

- White, NS et al. (2014) Diffusion-Weighted Imaging in Cancer: Physical Foundations and Applications of Restriction Spectrum Imaging. *Cancer Research*. 74(17):4638-52. doi: 10.1158/0008-5472.CAN-13-3534
- Rakow-Penner, RA et al. (accepted pending revisions) Novel Technique for Characterizing Prostate Cancer Utilizing MRI Restriction Spectrum Imaging: Proof of Principle and Initial Clinical Experience with Extra-Prostatic Extension. *Prostate Cancer Prostatic Diseases*.
- Liss, MA et al. (submitted). MRI-derived Restriction Spectrum Imaging Cellularity Index is Associated with High Grade Prostate Cancer on Radical Prostatectomy Specimens.

Diffusion-Weighted Imaging in Cancer: Physical Foundations and Applications of Restriction Spectrum Imaging

Nathan S. White, Carrie R. McDonald, Niky Farid, et al.

Cancer Res 2014;74:4638-4652.

Updated version Access the most recent version of this article at:
<http://cancerres.aacrjournals.org/content/74/17/4638>

Cited Articles This article cites by 82 articles, 17 of which you can access for free at:
<http://cancerres.aacrjournals.org/content/74/17/4638.full.html#ref-list-1>

E-mail alerts [Sign up to receive free email-alerts](#) related to this article or journal.

Reprints and Subscriptions To order reprints of this article or to subscribe to the journal, contact the AACR Publications Department at pubs@aacr.org.

Permissions To request permission to re-use all or part of this article, contact the AACR Publications Department at permissions@aacr.org.

Diffusion-Weighted Imaging in Cancer: Physical Foundations and Applications of Restriction Spectrum Imaging

Nathan S. White¹, Carrie R. McDonald², Niky Farid¹, Josh Kuperman¹, David Karow¹, Natalie M. Schenker-Ahmed¹, Hauke Bartsch¹, Rebecca Rakow-Penner¹, Dominic Holland¹, Ahmed Shabaik³, Atle Bjørnerud⁴, Tuva Hope⁵, Jona Hattangadi-Gluth⁶, Michael Liss⁷, J. Kellogg Parsons⁷, Clark C. Chen⁸, Steve Raman⁹, Daniel Margolis⁹, Robert E. Reiter¹⁰, Leonard Marks¹⁰, Santosh Kesari¹¹, Arno J. Mundt⁶, Christopher J. Kane⁷, Bob S. Carter⁸, William G. Bradley¹, and Anders M. Dale^{1,11}

Abstract

Diffusion-weighted imaging (DWI) has been at the forefront of cancer imaging since the early 2000s. Before its application in clinical oncology, this powerful technique had already achieved widespread recognition due to its utility in the diagnosis of cerebral infarction. Following this initial success, the ability of DWI to detect inherent tissue contrast began to be exploited in the field of oncology. Although the initial oncologic applications for tumor detection and characterization, assessing treatment response, and predicting survival were primarily in the field of neurooncology, the scope of DWI has since broadened to include oncologic imaging of the prostate gland, breast, and liver. Despite its growing success and application, misconceptions about the underlying physical basis of the DWI signal exist among researchers and clinicians alike. In this review, we provide a detailed explanation of the biophysical basis of diffusion contrast, emphasizing the difference between hindered and restricted diffusion, and elucidating how diffusion parameters in tissue are derived from the measurements via the diffusion model. We describe one advanced DWI modeling technique, called restriction spectrum imaging (RSI). This technique offers a more direct *in vivo* measure of tumor cells, due to its ability to distinguish separable pools of water within tissue based on their intrinsic diffusion characteristics. Using RSI as an example, we then highlight the ability of advanced DWI techniques to address key clinical challenges in neurooncology, including improved tumor conspicuity, distinguishing actual response to therapy from pseudoresponse, and delineation of white matter tracts in regions of peritumoral edema. We also discuss how RSI, combined with new methods for correction of spatial distortions inherent in diffusion MRI scans, may enable more precise spatial targeting of lesions, with implications for radiation oncology and surgical planning.

See all articles in this *Cancer Research* section, "Physics in Cancer Research."

Cancer Res; 74(17): 4638–52. ©2014 AACR.

Introduction

Diffusion-weighted imaging (DWI) is increasingly used as an imaging biomarker for the detection and characterization of primary and metastatic brain tumors as well as for prognostic

cation and monitoring treatment response in this patient population. The unique ability of this technique to probe the underlying structure of brain tissue at a cellular level makes it well poised to answer questions about tumor biology, as well as the microstructure of peritumoral white matter. The greatest enthusiasm to date has surrounded the ability of DWI to estimate tumor cellularity on the basis of quantitative images of diffusion, namely apparent diffusion coefficient (ADC) maps. In particular, numerous investigators have shown a negative correlation between tumor ADC values and cellularity (1–3), which is commonly attributed to increased restricted diffusion imposed by tumor cells. Following this logic, ADC has been used with varying success to characterize and grade primary and metastatic brain tumors (3–9), to assess tumor response to therapy (10–12), and to predict survival in patients with malignant tumors (13–17). However, confusion about the true biophysical basis of the DWI signal abounds, and awareness of the limitations of the existing approaches has led to the development of advanced DWI methods that extend beyond the tensor model. These methods include high-angular diffusion imaging techniques, such as diffusion spectrum imaging (DSI; ref. 18) and

¹Department of Radiology, University of California, San Diego, San Diego, California. ²Department of Psychiatry, University of California, San Diego, San Diego, California. ³Department of Pathology, University of California, San Diego, San Diego, California. ⁴Department of Physics, University of Oslo, Oslo, Norway. ⁵Department of Circulation and Medical Imaging, Norwegian University of Science and Technology, Trondheim, Norway. ⁶Department of Radiation Oncology, University of California, San Diego, San Diego, California. ⁷Department of Urology, University of California, San Diego, San Diego, California. ⁸Center for Theoretical and Applied Neuro-Oncology, Division of Neurosurgery, University of California, San Diego, San Diego, California. ⁹Department of Radiology, University of California, Los Angeles, Los Angeles, California. ¹⁰Department of Urology, University of California, Los Angeles, Los Angeles, California. ¹¹Department of Neurosciences, University of California, San Diego, San Diego, California.

Corresponding Author: N.S. White, University of California, San Diego, 9500 Gilman Drive #0841, La Jolla, CA 92093-0841. Phone: 858-534-8259; Fax: 858-534-1078; E-mail: nswhite@ucsd.edu

doi: 10.1158/0008-5472.CAN-13-3534

©2014 American Association for Cancer Research.

Q-ball imaging (19), as well as methods to probe non-Gaussian diffusion, including biexponential (20, 21), stretched exponential (22), and kurtosis imaging (23), and methods to study perfusion-related effects at low b -values, such as intravoxel incoherent motion (IVIM; ref. 24). Although these techniques often provide a better characterization of tissue architecture than traditional models, the relationship of these measures to the underlying pathophysiology of tumors is largely unknown.

Advances in magnetic resonance (MR) technology are now creating even more possibilities, increasing excitement in the field by broadening the potential applications of DWI within cancer diagnosis and treatment. Newer scanners with improved gradient performance allow for higher b -values with shorter diffusion and echo times. In addition, improved coil technology and higher field strength provide better signal-to-noise ratio (SNR). With these MR advancements, it has become possible to develop new, innovative DWI methods that provide more direct measures of tumor cellularity by leveraging the intrinsic contrast of tumor cells relative to other tissues. Such direct measures address a top challenge posed by the NCI to develop *in vivo* imaging methods that portray tumor "cytotypes," i.e., imaging methods that can probe the identity, quantity, and location of different cells that make up a tumor and its microenvironment (NIH RFA-CA-13-020). However, the successful application of such methods requires not only advanced MR technology and an appreciation of the clinical challenges in neurooncology, but also an exquisite understanding of the physical basis of the DWI signal and its current limitations.

The purpose of this review is to provide a detailed explanation of the biophysical basis of diffusion contrast and to demonstrate what is known about how it reflects tissue microstructure in the context of key clinical dilemmas in neurooncology. We begin with a basic introduction of how diffusion measurements are derived from DWI and then follow with a review of the biophysical properties of water diffusion in tissue. We then describe how diffusion parameters in tissue are derived from the measurements via fitting of the diffusion model to observed data. For this review, we focus on one advanced DWI modeling technique called restriction spectrum imaging (RSI), which provides a general framework for estimating tissue properties from DWI data and addresses the NCI challenge for more direct, *in vivo* imaging of tumor cells. We also address the power of multispectral imaging, highlighting the importance of combining advanced DWI methods such as RSI with other imaging modalities (i.e., MRI perfusion, PET) to optimize the detection and monitoring of brain tumors. Although the primary focus of this review is on the application of RSI to neurooncology, the same methods are equally applicable to other applications of oncologic imaging, such as prostate, liver, and breast cancer, and we briefly present some preliminary data in prostate cancer at the end of "clinical applications."

Principles of Diffusion MRI

The diffusion experiment

While early diffusion measurements using nuclear magnetic resonance (NMR) in biologic tissue were made in the 1960s and 1970s, it was not until the mid 1980s that the basic principles of DWI emerged (25–27). All MRI techniques, including DWI, rely

on the fundamental principle that water hydrogen nuclei become magnetized when placed in a strong static magnetic field. MRI contrast is formed by perturbing this magnetization using electromagnetic waves and then allowing the magnetization to "relax" back to an equilibrium state. Tissue relaxation times—namely, the spin–lattice (T_1) and spin–spin (T_2) relaxation times—form the fundamental basis of soft tissue contrast and anatomic imaging with MRI. DWI is an MRI technique that adds additional sensitivity to the intrinsic random thermal displacements of water molecules that take place during the MRI experiment as part of the natural diffusion process. A pair of pulsed magnetic field gradients are turned on and off in succession (with duration δ) to magnetically "label" and "refocus" the spin phase of hydrogen nuclei, depending on where they reside physically in the gradient field (Fig. 1). The second refocusing pulse is applied some finite time Δ after the first pulse in an effort to realign the spin phases of stationary nuclei. Thus, any residual spin phase left after the application of the refocusing pulse can be attributed to the diffusion of water along the orientation of the field gradient during the effective diffusion time of the experiment T_d , defined here as $\Delta - (\delta/3)$. The net phase dispersion due to diffusion causes an attenuation of the measured signal and a decrease in the voxel intensity. Stejskal and Tanner (28) were some of the pioneers of the pulsed field gradient experiment and provided the mathematic framework to relate the diffusion coefficient to the experimental variables. To date, the Stejskal Tanner pulse sequence remains the gold standard method for measuring diffusion in the clinic and forms the basis of quantitative mapping of tumor cellularity with ADC, as discussed below.

Biophysics of water diffusion in tissue

In this section, we provide a basic review of the three principal physical modes of diffusion in tissue: free, hindered, and restricted.

Free diffusion. Free water diffusion describes the random (Brownian) motion of water molecules due to thermal agitation, in the absence of any obstacles. The displacement distribution of free water molecules is time dependent and Gaussian and obeys a statistical law established by Einstein in 1905. Along a single direction in space, the average molecular excursion of water molecules is proportional to the square root of diffusion time T_d . Mathematically, this can be expressed as $s = (2DT_d)^{1/2}$, where s is the root-mean-squared distance and D is the diffusion coefficient (Fig. 2A). For free water at brain temperatures (37°C), the diffusion coefficient is approximately $3 \mu\text{m}^2/\text{ms}$ (29), which translates to a distance of approximately $17 \mu\text{m}$ in 50 milliseconds. In brain tissue, however, water molecules are constantly bouncing off and interacting with various tissue elements such as cell membranes and macromolecules. The net result is a decrease in diffusion mobility of water and a displacement distribution that no longer follows a single Gaussian distribution. Generally speaking, tissue elements impede water diffusion both through diffusion hindrance and restriction. Hindered and restricted diffusion are two distinct processes that result from fundamentally different behavior of spins within the intra- and extracellular tissue compartments, as described next.

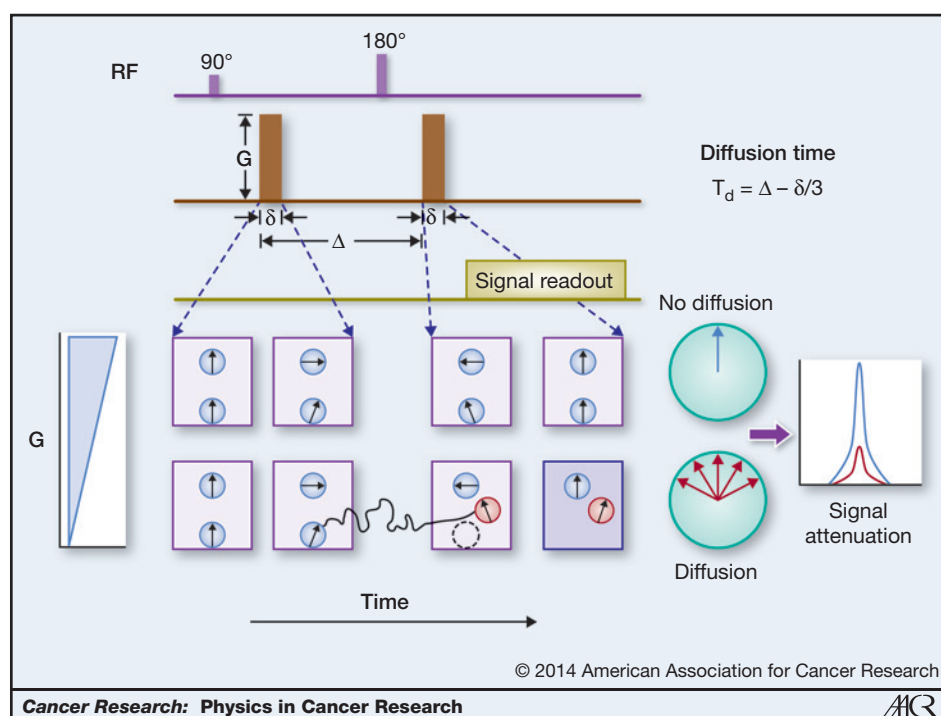


Figure 1. The diffusion experiment. Sensitivity to the random molecular displacements (Brownian motion) of water molecules is achieved through the use of two magnetic field gradient pulses with amplitude G , duration δ , and separation Δ . During the first pulse, the initial positions of water molecules (spins) are encoded with a phase offset, depending on their spatial location in the gradient field. The second pulse is then applied after some finite delay Δ to realign the spin phases. In this way, if water molecules diffuse to a different physical location along the gradient field direction, refocusing will be imperfect and a net phase dispersion will result. This phase dispersion causes an attenuation of the magnitude signal and a decrease (darkening) of the measurement voxel in the reconstructed image.

Hindered diffusion. Hindered diffusion refers to the delay of passage of small molecules as they navigate around cellular obstacles, as in brain extracellular space (ECS; Fig. 2B). There is a long history (30) of quantifying the degree of hindrance to diffusion in the ECS compared with that of a free medium by the tortuosity λ (31), defined simply as the square root of the ratio of the free (or intrinsic) extracellular diffusion coefficient D_{extra} to the measured or ADC for extracellular water $\text{ADC}_{\text{extra}}$: $\lambda = (D_{\text{extra}}/\text{ADC}_{\text{extra}})^{1/2}$. As such, tortuosity simply reflects the degree to which the ECS slows diffusion relative to free water. Extensive experimental studies using real-time iontophoresis (RTI) using the cation tetramethylammonium (TMA) indicate that diffusion through tortuous ECS in normal brain is generally slowed by a factor of about 2.6, corresponding to λ of about 1.6 (31). Although there may be several factors that ultimately contribute to the delay of passage of water molecules in brain ECS (such as the composition of the extracellular matrix and the transient trapping or binding of water molecules to cell surfaces; see ref. 32), perhaps the greatest contribution is ECS geometry (dictated by the extracellular volume fraction α and shape of cells). As α decreases, due to, for example, cell swelling or greater cell packing density (cellularity), water molecules must travel more circuitous paths around cellular obstructions and tortuosity increases. The maximum theoretical tortuosity due to geometry can be quantified as the ratio of the distance though the center of a spherical cell to the distance around the periphery of the cell or $\lambda_g = \pi/2 = 1.57$ (Fig. 2, inset). However, more complex simulations over a wide variety of packed cellular objects indicate that the maximum tortuosity due to geometry is no greater than 1.22 (33). In tumor ECS (or "tumor interstitium"), both tortuosity and volume fraction α are generally higher. For example, in anaplastic astrocytomas and glioblas-

tomas, the average α was measured to be as high as 0.47 to 0.49, with λ around 1.67 to 1.77 (34). Increased α has been associated with necrosis and/or vasogenic edema, whereas increased λ may result from either astrogliosis, commonly observed in tumor tissue, or to changes in the extracellular matrix (32, 34). In summary, while it is often suggested that the low ADC observed in high-grade tumors results from increased packing density (cellularity) of cells due to greater hindrance imposed on extracellular water diffusion, from a physical perspective, cellular crowding can only mildly reduce the effective diffusion coefficient in tumors (λ increases only narrowly with decreasing α). Therefore, it stands to reason that a major component in decreased ADC in tumors, especially at high b -values, is restricted diffusion within the cellular compartments themselves, described next.

Restricted diffusion. Restricted diffusion is a term classically used (35) to describe the trapping of water molecules within an enclosed compartment (i.e., as defined by the cell plasma membrane) such that the net distance traveled is restricted or confined by the compartment dimensions. Although the term "restricted diffusion" is often used in the clinical literature to refer to any reported decrease in ADC, the physics of restricted diffusion is fundamentally different from hindered or free water diffusion. Specifically, for restricted diffusion, the net squared displacement of water molecules is sublinear in time and therefore non-Gaussian (Fig. 2C). In addition, the time evolution of net displacements strongly depends on the size and shape of the restricting compartment as well as the intrinsic intracellular diffusivity D_{intra} . In contradistinction to hindered extracellular water, where $\text{ADC}_{\text{extra}}$ is independent with diffusion time T_d , the effective diffusion coefficient for intracellular water (or $\text{ADC}_{\text{intra}}$) decreases with

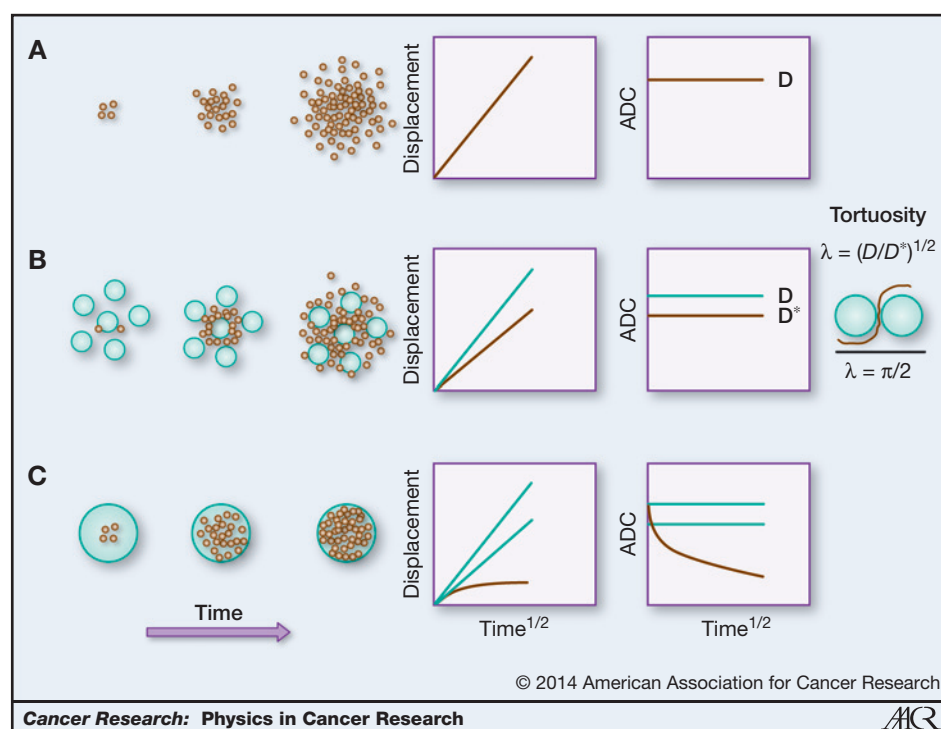


Figure 2. The three principal modes of diffusion in tissue. A, free diffusion; in free water, the average molecular excursion along a single dimension in space in terms of the root-mean-squared distance s increases linearly with the square root of diffusion time $s = (2DT_d)^{1/2}$ with a slope that depends on the intrinsic diffusivity D . B, hindered diffusion; for hindered water in brain ECS, the net displacements remain linear with the square root of diffusion time (i.e., Gaussian), but the effective diffusion coefficient D^* (or ADC) is reduced compared with D due to tortuosity of the ECS. The theoretical maximum reduction in D^* (or ADC) that can be expected due to crowding of small spherical cells in the ECS is given by the tortuosity limit $\pi/2$ or 40% (35). C, restricted diffusion; in restricted intracellular diffusion, the net distance traveled by water molecules is limited by the compartment dimensions, leading to a sublinear time evolution of the net squared displacement and a decreased ADC. The ADC of restricted intracellular water decreases with diffusion time as a larger proportion of the spins "bounce off" the plasma membrane.

T_d over a finite range as a larger proportion of the spins "bounce off" the plasma membrane.

It is important to note that restricted (or non-Gaussian) diffusion must be discussed within the context of diffusion time, permeability, and the size of the restricting cellular compartments. For instance, in the short-time limit ($T_d < 1$ ms), diffusion is largely unrestricted and dictated by the intrinsic diffusivity of the medium ($ADC_{intra} \sim D_{intra}$), except for a small minority of spins located in close proximity to cell membranes or other barriers. Conversely, in the long-time limit ($T_d > 1$ s), much greater than the average residence time for water within intra- and extracellular compartments, diffusion is dominated by exchange and can be accounted for by a single apparent tensor, reflecting the effective medium approximation of the tissue ($ADC_{intra} \sim ADC_{tissue}$). In the intermediate-time regimen, relevant to typical clinical DWI acquisitions ($T_d \sim 50$ – 100 ms), the diffusion time is short relative to exchange between intra- and extracellular compartments through the plasma membrane (36), but long enough for water molecules to repeatedly come in contact with and "bounce off" the plasma membrane. In this case, the intracellular spins approach a "fill-up" regimen, where the displacements of spins are physically restricted by the plasma membrane and, therefore, dictated by the size and shape of the cellular compartment. Note that in the intermediate-time regimen, diffusion in the ECS remains hin-

dered and behaves according to a classic Gaussian model, where the tortuosity is a function of packing density and extracellular volume fraction (31). Therefore, the total water signal in the intermediate-time regimen reflects a superpositioning of hindered and restricted water, leading to a non-monoexponential signal decay at high b -value. As we see below, separating the restricted water fraction from hindered and free water fraction provides a more sensitive and specific biomarker for tumor cellularity compared with traditional ADC.

Diffusion models

Diffusion models form the fundamental basis through which quantitative information about the underlying tissue microstructure can be gleaned from DWI signals. The typical millimetric scale at which DWI measurements are made (i.e., voxel size) is large compared with the micrometric scale of the underlying physical diffusion process, and, therefore, the goal of the diffusion model is to bridge the gap such that inference can be drawn on a scale much smaller than the voxel dimensions. One of the advantages of DWI over other MRI techniques is that the physical scale probed by the measurements can be adjusted by the experimental variables, namely the diffusion time (T_d) and diffusion-weighting factor (b -value). As we see, this forms the fundamental basis through which more advanced multiscale, or non-Gaussian, diffusion models offer

insight into compartmental diffusion in cancer and improved imaging biomarkers for tumors. We begin this section with brief introduction of the classic ADC and tensor model for Gaussian diffusion and follow it with a more detailed introduction to RSI, a technique developed in our laboratory for probing tissue microstructure in greater detail.

ADC. As a departure from earlier studies in which efforts were made to measure the true diffusion process in biologic systems (37), it was suggested in the mid 1980s (24) to model the complex diffusion in tissue using the free (Gaussian) diffusion equation, but replace the intrinsic diffusion coefficient D with a global statistical parameter called ADC. The ADC concept has since been used extensively in the literature as well as clinical oncology as a surrogate marker of tumor cellularity (1–3). In practice, the ADC is estimated by combining the experimental variables (i.e., the magnitude, duration, and temporal spacing of the diffusion gradients) into a single parameter called the diffusion-weighting factor, or b -value (24), and comparing the signal attenuation at one or more nonzero b -values with the baseline signal measured without diffusion weighting (i.e., with a b -value of zero). For Gaussian diffusion, the signal attenuation decays exponentially with the product of the b -value and ADC, and, therefore, the ADC reflects the slope of the best fit line to the log signal as a function of b -value. The diffusion tensor model (DTI) extends the ADC concept to three-dimensional space, allowing for different ADCs along and perpendicular to the principal axis of diffusion (38).

The main limitation of the ADC and tensor model as imaging biomarkers for tumors is their strict dependence on a single Gaussian function for the displacement distribution of water molecules within cancer tissue and, therefore, a monoexponential dependence on the b -value. Although a single Gaussian assumption may be appropriate for data collected over a fairly narrow range of b -values (up to about 1,000 s/mm²), the inferences that can be drawn are limited by lack of specificity. For example, numerous investigators have shown a negative correlation between the tumor ADC values and cellularity (1–3), which is commonly attributed to increased restricted diffusion imposed by tumor cells. However, despite increased restricted diffusion, tumor ADC values rarely fall below that of normal appearing white matter (NAWM). This is true even in highly cellular tumors that originate in white matter, such as glioblastoma multiforme (GBM) and primary CNS lymphoma (39). One explanation for higher than expected ADC values in these tumors is the presence of vasogenic edema and focal necrosis within the tumor itself, which increases the ADC through reduced hindrance imposed on the extracellular water (40, 41). Thus, increased ADC due to edema and necrosis will offset reduced ADC imposed by tumor cells, resulting in lesions that are difficult to discern from NAWM on the basis of the ADC alone. This effect becomes more pronounced as the b -value is reduced because of increasing sensitivity to the fast, hindered water fraction.

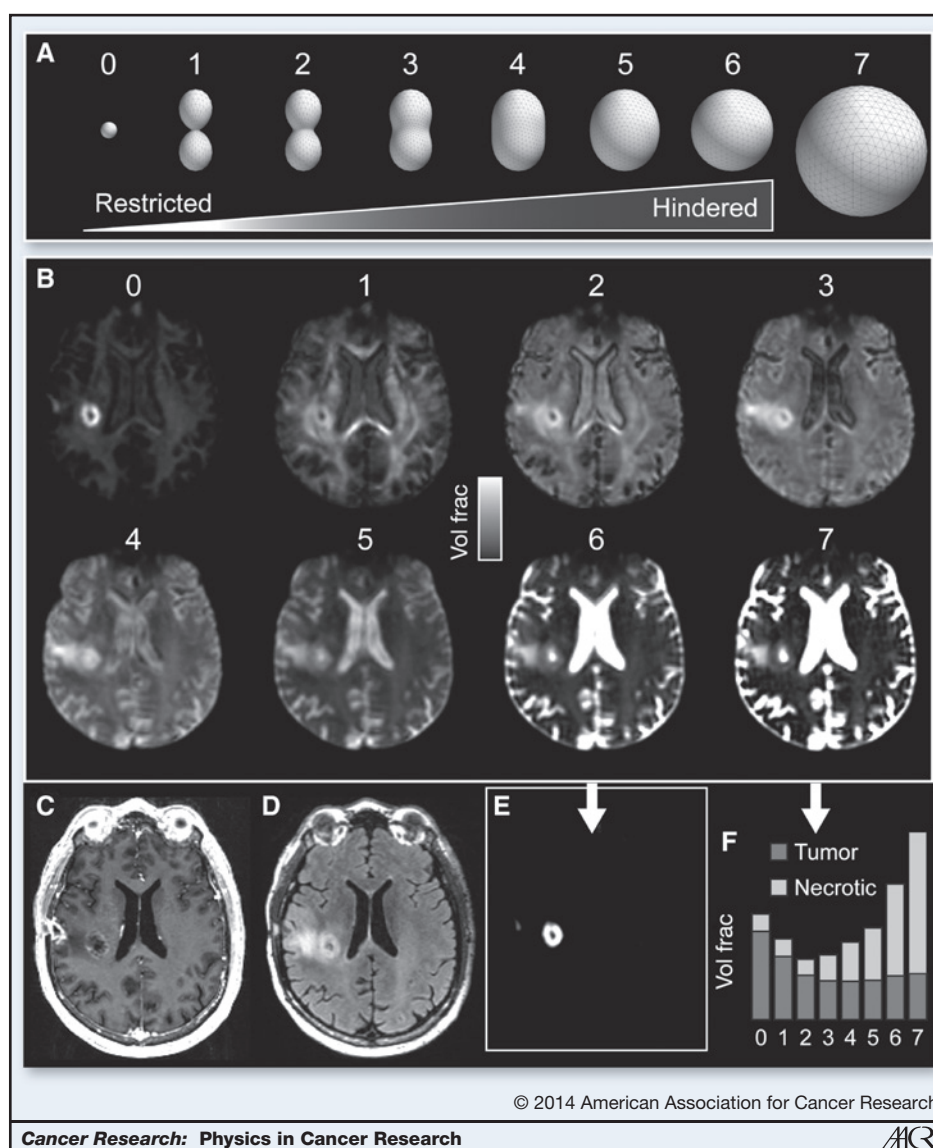
RSI. Over the past decade or so, advances in DWI acquisition and gradient hardware have made it possible to probe a whole new regimen of water diffusion in cancer tissue beyond what was previously possible on clinical MRI scanners. Specifically, the application of strong magnetic field gradient

pulses has allowed a much greater range of b -values, diffusion directions, and diffusion times to be acquired during a clinical acquisition. As a result, diffusion signals can be made specific to pools of water with very low effective diffusion coefficients, well below the tortuosity limit for ECS water, likely originating from restricted water trapped within the cells themselves (42). Numerous promising methods are emerging to capture and model complex non-Gaussian diffusion in tissue, including biexponential (20, 21), stretched exponential (22), and kurtosis models (23), as well as methods to study perfusion-related effects in DWI data at low b -values, such as IVIM (24). The application and description of many of these techniques for neurooncology applications can be found in an excellent review provided by Maier and colleagues (39). Moreover, techniques are emerging to probe diffusion spectra at ultra-short diffusion times on clinical systems using oscillating gradients (43), which hold promise for probing intracellular structures and alterations in cancer (44). For this review, we focus on one particular technique developed in our laboratory called RSI. Over the last few years, RSI has gained increased recognition as an important tool in oncology that overcomes many of the limitation of traditional DWI and ADC.

RSI is a general framework for modeling diffusion signals collected across a broad range of experimental parameters and relating these signals to underlying tissue parameters (e.g., size and shape/orientation of hindered and restricted water compartments) using a linear mixture model (45). The ultimate goal of RSI is to enable quantitative estimates of tissue microstructure based on noninvasive imaging. To achieve this, the diffusion signal is modeled as reflecting a mixture of components, where each component describes the signal dependence on specific tissue properties (e.g., cell size, density, orientation, etc.) as a function of the experimental (protocol) settings (e.g., b -value, diffusion time, echo time, etc.). The total signal becomes the weighted sum of these components, and the goal is to determine the individual weights. This is achieved through the application of generalized linear estimation techniques (45, 46). As such, the RSI framework is designed to strike a balance between model complexity and interpretability by minimizing *a priori* assumptions on microstructure while preserving biophysical interpretability of the resulting estimates.

Our current clinical implementation of RSI acquires data with b -values of 500, 1,500, and 4,000 s/mm² and multiple diffusion directions at each b -value at a fixed intermediate diffusion time (~90 ms), where intracellular spins would be expected to be in the fill-up regimen. The RSI design matrix includes a distribution (or "spectrum") of effective diffusion pools spanning hindered and restricted length scales with both isotropic and anisotropic geometries. In Fig. 3, we illustrate both a schematic for the RSI spectrum model and the resultant fit of the model to data collected in a 51 year-old patient with right frontal GBM before surgical intervention (47). Note the separation of diffusion components in different tissue types, with the primary lesion exhibiting a large volume fraction of spherically restricted water, likely stemming from water trapped within cancer cells. Also note the large fraction of free and hindered water in areas of necrosis and edema. The volume fraction of spherically restricted water (either with or

Figure 3. RSI analysis of a 51 year old male with right frontal GBM. A, illustration of the RSI "spectrum" model used to fit the multi- b -value, multidirection DWI data. Scales 0–2 and 3–6 correspond to restricted and hindered diffusion, respectively. Scales 0, 6, and 7 are isotropic, whereas scales 1–5 are anisotropic (i.e., oriented). B, RSI-derived (T_2 -weighted) volume fraction maps for each scale in A. C, T_1 -weighted postcontrast (D) T_2 -weighted FLAIR (E) RSI-derived "cellularity map" (RSI-CM) corresponding to a weighted ("beamformed") linear combination of scales 0–7 showing maximal sensitivity and specificity to spherically restricted diffusion (scale 0). F, bar plot of volume fractions for two representative voxels in tumor and necrotic tissue, respectively.



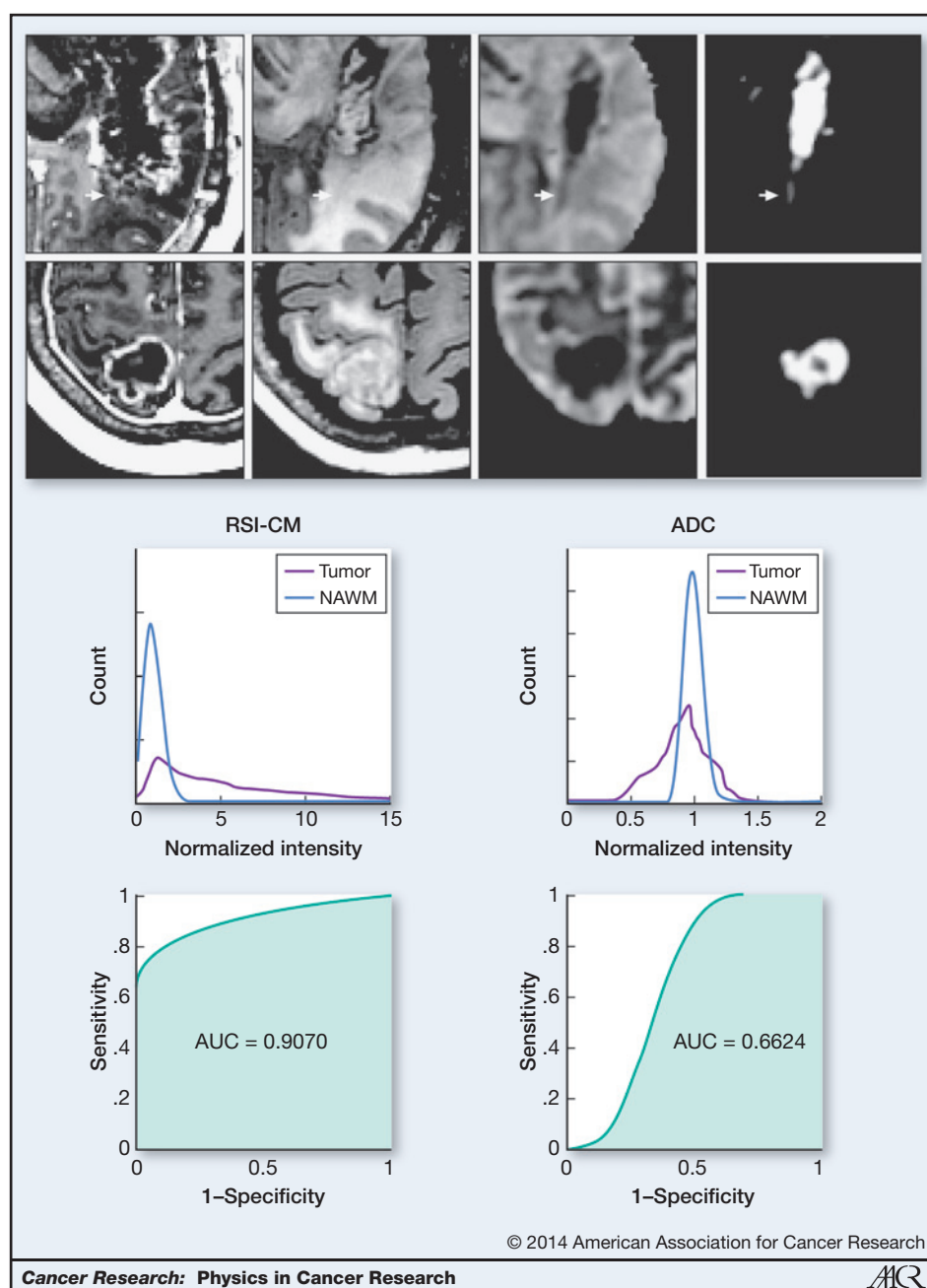
without additional filtering of white matter signal using a technique called "beamforming"; ref. 48) has been coined the RSI cellularity index or cellularity map (47, 49–51). In addition, the signal from the restricted anisotropic component can be used to map the density and orientation of surrounding white matter tracts (50).

In summary, advanced DWI methods such as RSI that acquire data over an extended b -value range provide the ability to quantify complex non-Gaussian diffusion in tissue (21–23, 45, 52). Although these emerging techniques offer a new class of cancer imaging biomarkers, there remain many unanswered questions and tremendous opportunity for further advancing the field. Of particular importance is to understand exactly how parameters of the diffusion model relate to specific properties of cancer tissue, such as tumor cell size, density, and nuclear volume fraction. How specific are these biomarkers to tumor cells versus healthy or inflammatory cells? Can these new imaging biomarkers characterize tumor cytotypes and

address a top challenge posed by the NCI to develop *in vivo* imaging methods that can probe the identity, quantity, and location of different cells that make up a tumor and its microenvironment? (NIH RFA-CA-13-020). Finally, to what extent can these new imaging biomarkers help solve current clinical dilemmas in oncology such as distinguishing tumor recurrence from radiation injury? Answering these questions will undoubtedly require both advances in diffusion modeling, simulation, and MRI hardware and software [such as the latest ultra-high performance ("connectome") MRI scanners; ref. 53] together with improved quantitative histology, multimodal image registration, and validation procedures.

Clinical Applications of RSI

Because of its ability to isolate areas of truly restricted diffusion by separating and removing the hindered diffusion signal, RSI offers a more direct measure of tumor cells than other diffusion-weighted methods. Within the past year, we



have shown that by identifying areas of restricted diffusion, RSI can be applied clinically to (i) improve tumor conspicuity in patients with high-grade primary and metastatic brain tumors (47), (ii) facilitate the interpretation of tumor response on imaging following antiangiogenic treatments that significantly reduce edema (49), and (iii) improve the ability to visualize white matter pathways coursing through regions of peritumoral edema relative to standard DTI (50). In the following sections, we describe each of these clinical applications in further detail. In addition, we describe a clinical scenario in which RSI lacks specificity and a multispectral imaging approach is warranted.

Improved conspicuity of high-grade tumors with RSI

As described in the Introduction, ADC is frequently used as a marker of tumor cellularity in patients with high-grade tumors (1–3). Areas of tumor are associated with decreased ADC relative to surrounding tissue (40). However, concomitant edema and tumor-related necrosis increase ADC values, thereby directly opposing the reduction in ADC associated with tumor (54, 55). This offset presents a diagnostic challenge by diminishing the conspicuity of tumor on ADC maps. Because RSI isolates areas of spherically restricted diffusion, we tested whether it could provide increased conspicuity and delineation of tumor margins relative to standard and high *b*-value ADC

(47). To accomplish this, RSI was performed in ten presurgical patients: four with GBM, three with primary CNS lymphoma, and three with metastatic brain tumors. Tumor conspicuity, edema conspicuity, and relative sensitivity to edema were quantified for RSI cellularity maps (RSI-CM), high b -value DWI ($b = 4,000$), and ADC, and these values were compared in manually drawn volumes of interest. Receiver operating characteristic (ROC) curves were used to evaluate the sensitivity and specificity of each method for delineating tumor from NAWM. In addition to visible differences in conspicuity (Fig. 4), ROC curves revealed greater sensitivity and specificity for delineating tumor from NAWM with RSI-CM (AUC = 0.91) compared with both high b -value DWI (AUC = 0.77) and ADC (AUC = 0.66). In addition, the relative sensitivity to edema was greater for high b -value DWI and ADC compared with RSI, reflecting RSI's ability to suppress the fast diffusion component associated with edema. Furthermore, greater heterogeneity of the diffusion signal within the tumor was observed on the RSI-CMs compared with DWI and ADC, as evidenced by a broader

histogram distribution. This may represent the intrinsic heterogeneity of tumor cellularity both within and across tumor types. These data demonstrate one promising application of RSI, i.e., improved conspicuity and delineation of high-grade tumors compared with traditional DWI models and underscore the possibility that RSI may prove helpful in delineating tumor cytotypes and infiltrating disease in peritumoral edema.

RSI in the context of antiangiogenic treatment

Antiangiogenic therapies, such as bevacizumab, are increasingly used in the treatment of recurrent high-grade gliomas. However, these agents decrease permeability of the blood-brain barrier and, therefore, decrease contrast enhancement and edema in patients with high-grade gliomas in a manner that may not correlate with actual tumor response—a phenomenon known as pseudoresponse (56). Given this imaging challenge, we evaluated the ability of RSI to improve conspicuity within regions of the tumor compared with ADC in patients treated with bevacizumab and to further demonstrate

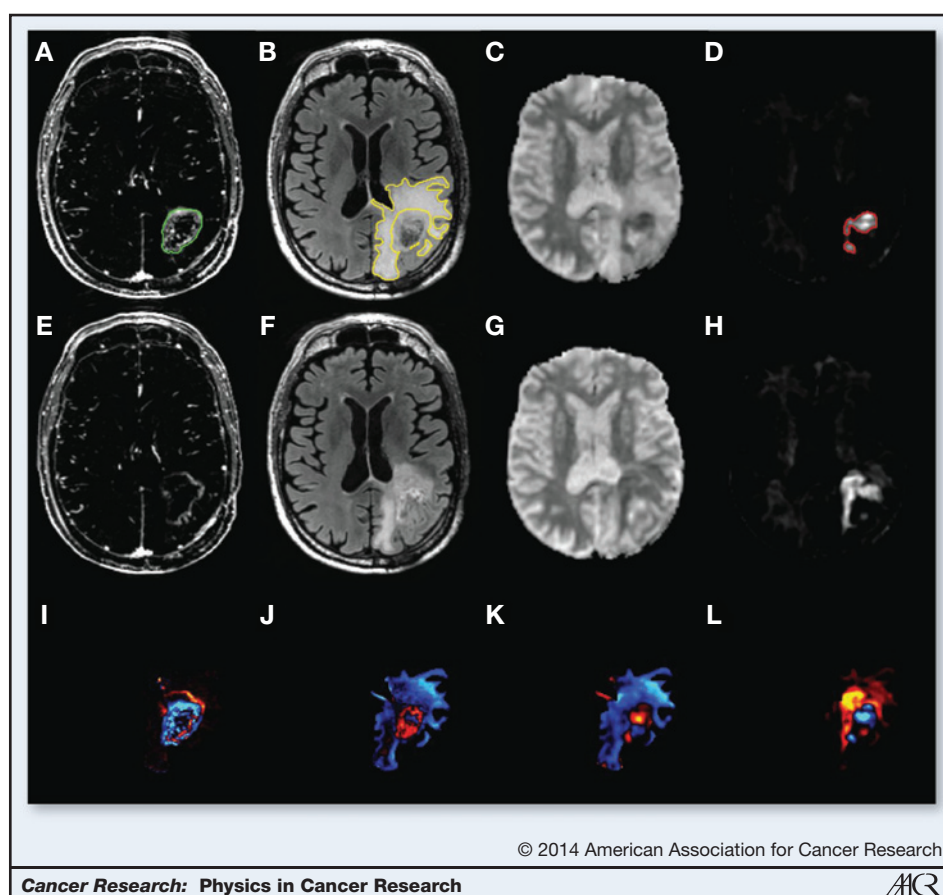


Figure 5. A 67 year old male with left parietal GBM status postresection and chemoradiation. Top, the T_1 postcontrast – T_1 precontrast (A), FLAIR (B), ADC (C), and RSI-CMs (D) before the start of bevacizumab; middle, T_1 postcontrast – T_1 precontrast (E), FLAIR (F), ADC (G), and RSI-CMs (H) after initiation of bevacizumab. Arrowheads, contrast-enhancing region (green), the surrounding region of FLAIR hyperintensity (yellow), and the region of restricted diffusion on RSI-CMs (red). Although there is a decrease in contrast enhancement and surrounding FLAIR hyperintensity after initiation of bevacizumab, the region of restricted diffusion increases and becomes more confluent, suggesting worsening residual/recurrent tumor. Moreover, this increase in the region of restricted diffusion is much more conspicuous on the RSI-CMs compared with the ADC. Bottom row depicts these changes on "change maps" (change in T_1 postcontrast – precontrast; I), change in FLAIR (J), change in ADC (K), and change in the RSI-CMs (L), with red–yellow indicating an increase in signal intensity and blue–cyan indicating a decrease in signal intensity. Of note, on the ADC change map (K), the area of increased restricted diffusion is essentially masked by the decreased signal intensity within the region of surrounding FLAIR hyperintensity.

that RSI is minimally affected by bevacizumab-induced reductions in edema (49). RSI-CMs and DWI were available for a series of patients with recurrent gliomas at baseline and following initiation of bevacizumab. Results showed that all patients exhibited sharp decreases in contrast enhancement and edema following treatment (i.e., pseudoresponse). Bevacizumab-induced decreases in edema had a greater effect on ADC than on the RSI-CMs, with the relative sensitivity to changes in edema being more than 20 times higher on ADC than on RSI-CMs (Fig. 5). These data provide additional evidence that RSI is less influenced by changes in edema compared with ADC, which may confer an advantage of RSI for interpreting true tumor response in the setting of anti-angiogenic treatment. However, this study did not include clinical follow-up. Thus, whether RSI has greater predictive validity than ADC is of key importance and requires additional investigation.

RSI for improved delineation of white matter tracts

There is increasing enthusiasm for the use of DTI and tractography in neurosurgical planning (57–64), and there is some evidence that tractography-guided neuronavigation can be used to minimize neurologic morbidity (60, 65, 66). However, the ability to resolve white matter structure in peritumoral regions that include edema has remained a challenge (39, 67). We applied the same logic as in the previous examples and tested the ability of RSI to provide better visualization and quantification of white matter tracts in regions that include edema (50). In this example, isolating the slow, restricted compartment yields a better estimate of "tubularity" (i.e.,

models the cylindrically restricted diffusion within axons; Fig. 3B, scale 1; ref. 45). This increases the sharpness of the estimates, allowing for better delineation of fiber tract orientation. In a series of ten patients with high-grade gliomas, we were able to demonstrate that RSI yielded higher fractional anisotropy (FA) estimates in regions of edema relative to standard DTI. Furthermore, at follow-up when the edema had resolved in most patients, FA estimates increased with DTI, but remained stable with RSI, indicating that FA estimates based on DTI were artificially suppressed by the edema. Tractography performed within regions of edema revealed superior ability of RSI to track fibers through areas of significant edema relative to standard DTI (Fig. 6). These data address yet another important and growing application of diffusion imaging within the field of neurooncology (i.e., surgical planning) and speak to the advantage of using advanced DWI models for revealing the anatomic structure of peritumoral white matter. An important caveat to mention is that it is well known that gliomas grow via an infiltrative pattern and that there is often nonenhancing infiltrating tumor surrounding the enhancing portion of a high-grade glioma (68). Further investigation is required to determine whether RSI or other advanced DWI methods will prove useful for detecting these areas of tumor infiltration.

Importance of a multispectral imaging approach

Despite the many recent advancements in MR technology and DWI methods, no single modality has emerged as the "holy grail" of tumor imaging. Thus, most diagnostic challenges in neurooncology are best addressed using a multispectral

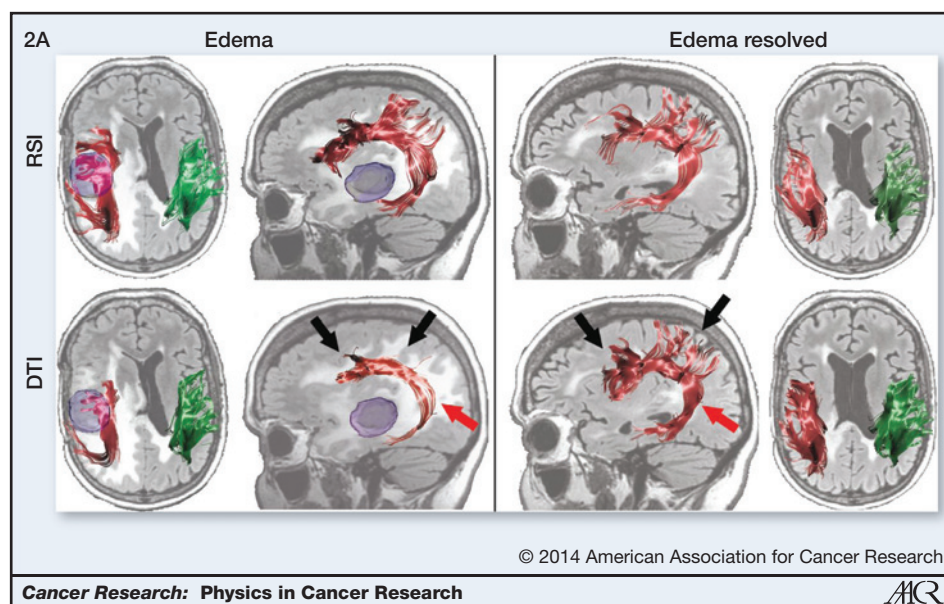
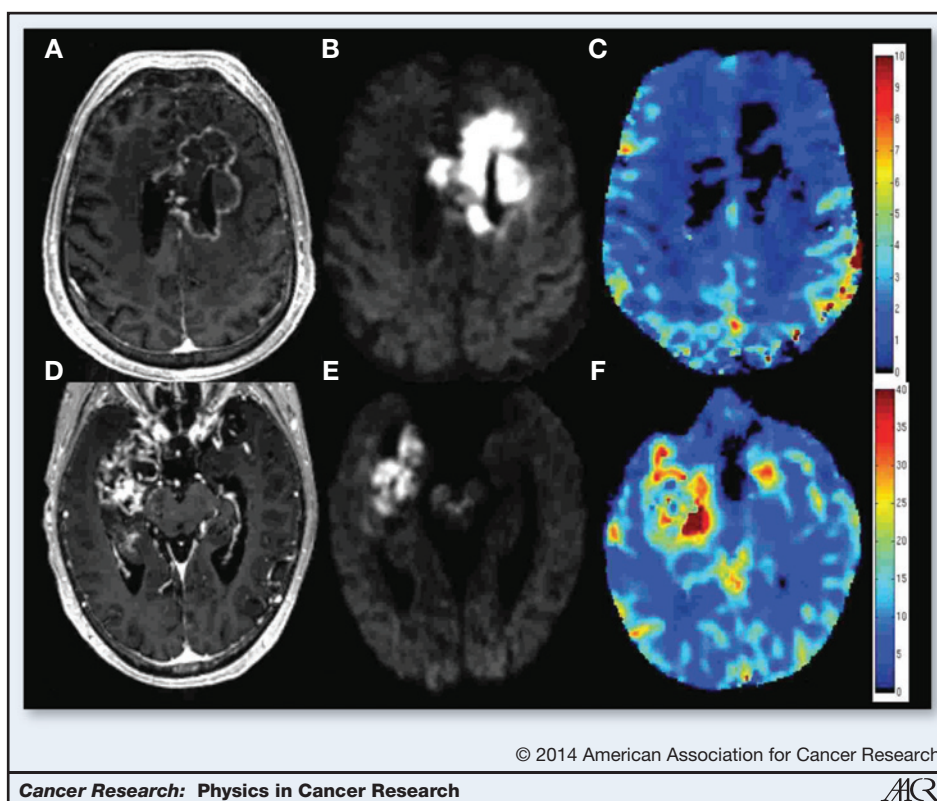


Figure 6. Streamline tractography of the superior longitudinal fasciculus for a 58 year old female with a right temporal lobe GBM projected onto baseline and follow-up FLAIR images. Left, RSI and DTI-based tractography at baseline in regions of edema; right, data obtained using the same tractography algorithm once the edema had mostly resolved. The ipsilateral (red) and contralateral (green) 3D renditions of the superior longitudinal fasciculus are superimposed on axial and sagittal FLAIR slices collected at each time point. The GBM is shown in blue in the preoperative image. With RSI, the superior longitudinal fasciculus appears very similar at baseline and at follow-up. However, with DTI, the superior longitudinal fasciculus appears thinner and truncated at baseline in regions of edema. Black arrows, frontal and parietal regions of the superior longitudinal fasciculus that terminate completely in regions of edema; red arrow, sparse streamlines in the temporal portion of the superior longitudinal fasciculus. These streamlines are "recovered" using DTI once the edema resolves.

Figure 7. Comparison of a 55 year old male with GBM treated with chemoradiation and bevacizumab (top) and a 66 year old male with GBM before any treatment (bottom). T₁ postcontrast images (A and D), RSI maps (B and E), and rCBV maps (C and F) are shown. Degree and homogeneity of restricted diffusion is greater in the patient treated with bevacizumab than in the pretreatment GBM control (images scaled identically with same window and level), whereas rCBV in the region of restricted diffusion is remarkably low in the patient treated with bevacizumab—lower than in the GBM control and lower than in the NAWM.



imaging approach. One particular challenge occurs following treatment with concurrent bevacizumab and radiotherapy, with a subset of patients developing regions of marked and persistent restricted diffusion that do not seem to reflect an aggressive tumor (69–71). Although the etiology of these lesions remains uncertain, pathologic confirmation in several patients has revealed atypical gelatinous necrosis. We have coined this abnormality bevacizumab-related imaging abnormality (BRIA) and have observed that the BRIA signal on RSI is quantitatively similar to that seen in a tumor (51). This illustrates a clinical scenario in which RSI lacks specificity and a multispectral imaging approach is warranted. Thus, we explored whether using RSI in combination with perfusion imaging could help to differentiate BRIA from recurrent tumor. In a series of patients, we show that these techniques are complementary in that RSI is superior to rCBV for differentiating pathology from NAWM, whereas rCBV is superior for differentiating BRIA from tumor (Fig. 7). Thus, the combination of high RSI signal and low rCBV provides a distinct imaging signature of the BRIA phenomenon. Because of the increasing use of antiangiogenic agents, imaging methods that increase our understanding of both pseudoresponse and BRIA are of high importance. These data highlight an important example in which RSI lacks specificity in its current instantiation, and information from complementary imaging modalities is essential.

RSI for improved detection of other solid organ tumors

Although this review is primarily focused on neurooncology applications, quantitative imaging is equally relevant to other

solid organ tumors. For example, multiparametric MRI has been explored in a variety of applications, including discrimination between indolent and aggressive disease in prostate cancer. Routine T_2 -weighted imaging of the prostate is the most sensitive way to evaluate anatomic detail, but is limited for disease detection, with sensitivity of around 70% and specificity of 55% (72). Functional MR techniques enhance detection, grading, and staging of prostate cancer through the use of dynamic contrast enhancement (DCE), DWI, and MR spectroscopic imaging. DCE requires intravenous administration of a T_1 -shortening agent with the chief limitation being that the maximum contrast enhancement between malignant and nonaggressive disease is small (73). MR spectroscopic imaging increases specificity (74, 75), but is technically challenging and can add significantly to scan time.

Multiple studies have shown that DWI improves sensitivity and specificity in the diagnosis of prostate cancer by increasing tumor conspicuity on DWI or quantitative ADC maps. However, hemorrhage, inflammatory processes, and benign nodules in the transitional zone can all exhibit lower ADC values, leading to false positives (76). DWI can also suffer from severe spatial distortion, limiting its coregistration to anatomic images, which is necessary for tumor localization.

Increasing Gleason score correlates with loss of normal gland formation, loss of peripheral gland tubular structure, and increased cellularity (77). We hypothesize, therefore, that RSI cellularity will correlate with higher tumor grade, as measured by Gleason score, and will provide significantly greater accuracy in discriminating aggressive tumors from

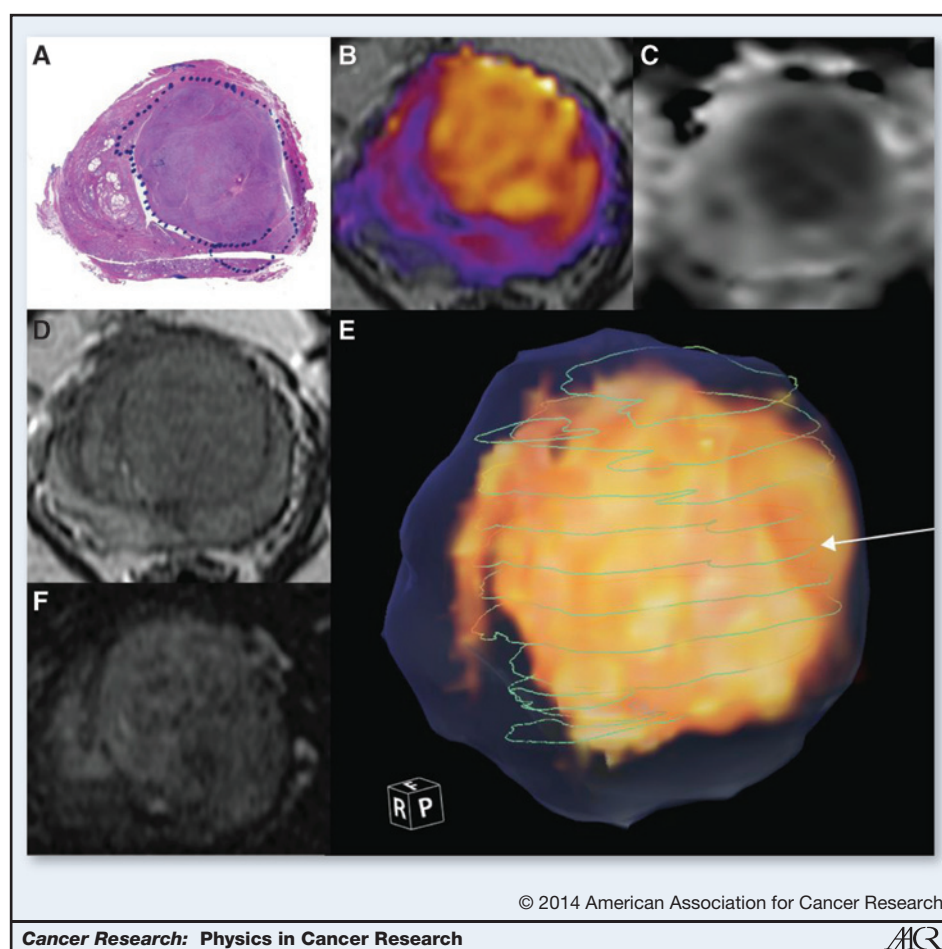


Figure 8. Gleason 3+4. A, histology section stained with hematoxylin and eosin. Blue dotted line, the boundary of the tumor. B, RSI cellularity map, color-coded and overlaid on T₂. C, ADC image. D, T₂ image. E, 3D volume rendering of the RSI (in yellow), the whole extent of the prostate as traced on T₂ images (translucent blue), and green lines indicating the boundary of the tumor on each of the whole-mount histologic sections that were compared with the RSI. The white arrow indicates the line corresponding to the histology section shown in A. F, raw perfusion data.

benign and indolent lesions when compared with current functional or anatomic imaging techniques.

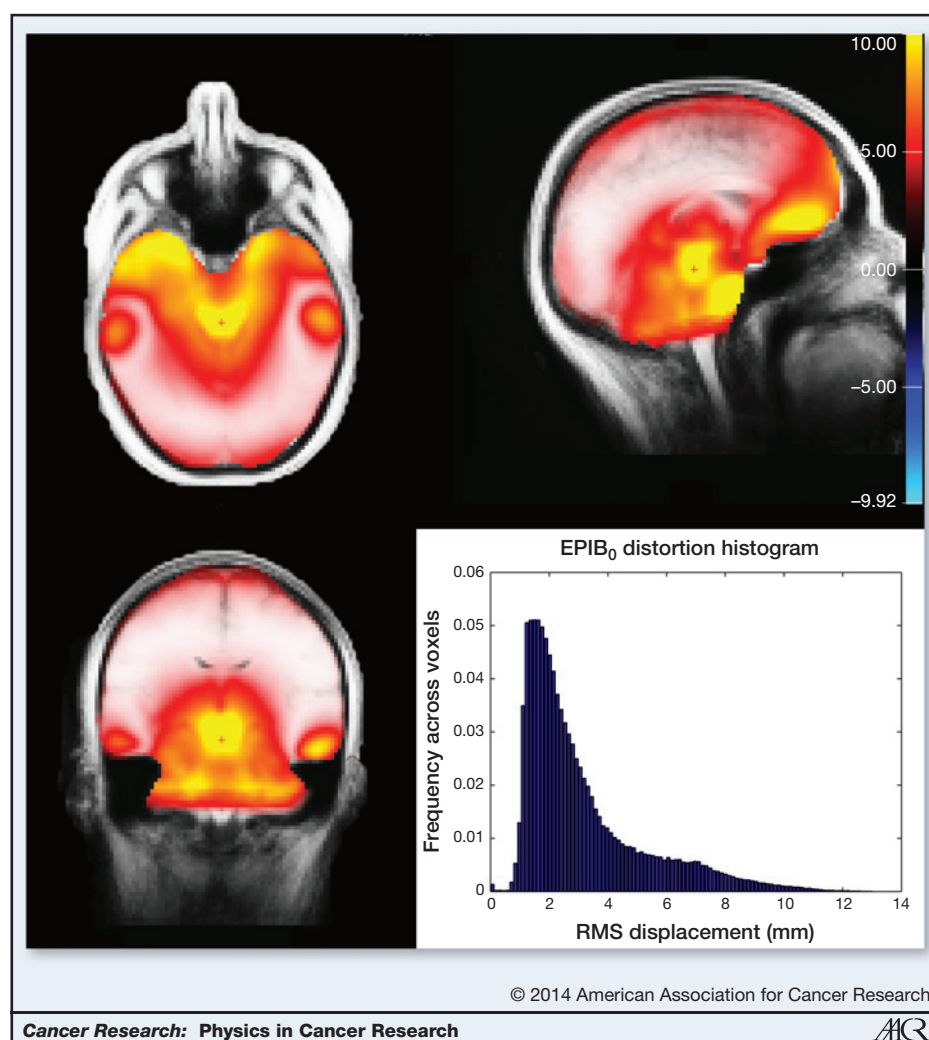
Our preliminary data are encouraging. Figure 8 shows a patient with Gleason 3+4 = 7 disease. RSI cellularity map is shown color-coded and fused with the T₂ after spatial distortion correction and registration. Note the correspondence of RSI cellularity with the histopathology slice. T₂ and perfusion images are not as conspicuous, with much less contrast-to-noise ratio. This represents an example case in which conventional imaging is not as diagnostic.

Importance of spatial distortion correction for accurate image-guided intervention

One of the main limitations of diffusion imaging in general is nonlinear spatial distortion of the images due to a number of factors, including gradient nonlinearities, eddy currents, and B₀ field inhomogeneities. Although distortions due to nonlinearities of the gradient fields are commonly corrected for by software on the scanner console, B₀ field inhomogeneities are not, despite being the dominant source of spatial inaccuracy in DWI. The magnitude of B₀ distortions varies depending on a number of factors, including field strength, positioning of the subject within the scanner, and subject-specific anatomy. The typical pattern of B₀ distortion on 3T systems is illustrated

in Fig. 9, along with the total whole-brain histogram of root mean square (RMS) displacements. As illustrated in the figure, on average (based scans from on 40 subjects) the typical (mode) distortion magnitude is approximately 2 mm, with a substantial proportion of voxels displaced more than 6 mm. Such distortions are of particular concern when images are used for image-guided intervention, including surgery, biopsy, or radiation dose planning. Although methods for correcting B₀ distortions have existed for some time (78–80), they are typically used only in research studies and not in clinical practice, primarily due to the additional scan time required to acquire the B₀ field maps required for standard correction methods. The method introduced by Holland and colleagues (81) overcomes this limitation by requiring only a single additional TR (2–3 seconds), using the reverse phase–encode polarity method (79, 82, 83). Moreover, this additional volume acquisition can be integrated directly in the native DWI protocol without changing the pulse sequence. Combined with efficient post-processing methods to estimate the distortion field (81), the reverse phase–encode polarity technique provides a much needed clinical solution for accurate spatial distortion correction of DWI data. The RSI technique incorporates this procedure as part of standard preprocessing of data, and all the data presented in this review has been corrected in this manner.

Figure 9. Three-plane map and histogram of the RMS displacement of voxels (in mm) due to B_0 distortions for axially acquired EPI images (A/P phase encoding) from EPI scans of a 40 normal healthy subjects.



Discussion and Conclusion

The field of MR imaging is rapidly evolving, leading to new and exciting possibilities within neurooncology, urologic oncology, and beyond. In particular, the development of advanced DWI methods has allowed for improved visualization and detection of tumor cells and, thus, has great potential for better understanding of tumor biology. Numerous clinical applications of this powerful technique have already been demonstrated, including tumor characterization and grading, prognostication, early prediction of response to therapy and survival, distinguishing tumor from treatment-related confounds, detecting microinfiltration, and guiding neurosurgical and radiation planning (84). However, future advances in the field will require a fundamental understanding of the underlying DWI signal coupled with validation of diffusion contrast in unique tumor-related pathologies. In addition to improved detection of tumors, advanced diffusion methods such as RSI may also provide quantitative characterization of cellular properties such as cell size, permeability, and nuclear volume fraction, based on signal variation as a function of diffusion

time and echo time (42). Validation of these measures will likely be borne out of translational efforts that include both preclinical and clinical studies in which histologic specimens are carefully coregistered to *in vivo* imaging. The need for targeted biopsies based on advanced DWI, precise coregistration of DWI with other imaging modalities, and careful corrections for geometric distortions will all be pivotal to providing the spatial precision needed to achieve such validation. These requirements underscore the need for a multidisciplinary approach to this validation including experts in the fields of oncology, surgery, pathology, and radiology. Through this collaboration, not only will current applications of DWI be further improved, but new possibilities will also be created that will ultimately lead to better care for patients suffering from cancer.

Disclosure of Potential Conflicts of Interest

D. Holland has ownership interest in patent #8,160,319 (reducing distortion in magnetic resonance images). A. Bjørnerud is a board member of NordicNeuroLab AS. D. Margolis received a commercial research grant from Siemens Medical Systems. A.M. Dale received a commercial research grant from General Electric Healthcare and has ownership interest (including

patents) in CorTech Labs, Inc. No potential conflicts of interest were disclosed by the other authors.

Acknowledgments

The authors thank the patients at University of California, San Diego, Neuro-Oncology Program for their generous participation.

References

- Sugahara T, Korogi Y, Kochi M, Ikushima I, Shigematu Y, Hirai T, et al. Usefulness of diffusion-weighted MRI with echo-planar technique in the evaluation of cellularity in gliomas. *J Magn Reson Imaging* 1999;9:53–60.
- Chen J, Xia J, Zhou YC, Xia LM, Zhu WZ, Zou ML, et al. [Correlation between magnetic resonance diffusion weighted imaging and cell density in astrocytoma]. *Zhonghua Zhong Liu Za Zhi* 2005;27:309–11.
- Guo AC, Cummings TJ, Dash RC, Provenzale JM. Lymphomas and high-grade astrocytomas: comparison of water diffusibility and histologic characteristics. *Radiology* 2002;224:177–83.
- Hilario A, Ramos A, Perez-Nunez A, Salvador E, Millan JM, Lagares A, et al. The added value of apparent diffusion coefficient to cerebral blood volume in the preoperative grading of diffuse gliomas. *AJNR Am J Neuroradiol* 2012;33:701–7.
- Server A, Kulle B, Maehlen J, Josefsen R, Schellhorn T, Kumar T, et al. Quantitative apparent diffusion coefficients in the characterization of brain tumors and associated peritumoral edema. *Acta Radiol* 2009;50:682–9.
- Toh CH, Castillo M, Wong AM, Wei KC, Wong HF, Ng SH, et al. Primary cerebral lymphoma and glioblastoma multiforme: differences in diffusion characteristics evaluated with diffusion tensor imaging. *AJNR Am J Neuroradiol* 2008;29:471–5.
- Wang W, Steward CE, Desmond PM. Diffusion tensor imaging in glioblastoma multiforme and brain metastases: the role of p, q, L, and fractional anisotropy. *AJNR Am J Neuroradiol* 2009;30:203–8.
- Wang S, Kim S, Chawla S, Wolf RL, Zhang WG, O'Rourke DM, et al. Differentiation between glioblastomas and solitary brain metastases using diffusion tensor imaging. *Neuroimage* 2009;44:653–60.
- Yamasaki F, Kurisu K, Satoh K, Arita K, Sugiyama K, Ohtaki M, et al. Apparent diffusion coefficient of human brain tumors at MR imaging. *Radiology* 2005;235:985–91.
- Tomura N, Narita K, Izumi J, Suzuki A, Anbai A, Otani T, et al. Diffusion changes in a tumor and peritumoral tissue after stereotactic irradiation for brain tumors: possible prediction of treatment response. *J Comput Assist Tomogr* 2006;30:496–500.
- Schminda KM. Diffusion-weighted MRI as a biomarker for treatment response in glioma. *CNS Oncol* 2012;1:169–80.
- Babsky AM, Hekmatyar SK, Zhang H, Solomon JL, Bansal N. Predicting and monitoring response to chemotherapy by 1,3-bis(2-chloroethyl)-1-nitrosourea in subcutaneously implanted 9L glioma using the apparent diffusion coefficient of water and ²³Na MRI. *J Magn Reson Imaging* 2006;24:132–9.
- Oh J, Henry RG, Pirzkall A, Lu Y, Li X, Catalaa I, et al. Survival analysis in patients with glioblastoma multiforme: predictive value of choline-to-N-acetylaspartate index, apparent diffusion coefficient, and relative cerebral blood volume. *J Magn Reson Imaging* 2004;19:546–54.
- Pope WB, Lai A, Mehta R, Kim HJ, Qiao J, Young JR, et al. Apparent diffusion coefficient histogram analysis stratifies progression-free survival in newly diagnosed bevacizumab-treated glioblastoma. *AJNR Am J Neuroradiol* 2011;32:882–9.
- Nakamura H, Murakami R, Hirai T, Kitajima M, Yamashita Y. Can MRI-derived factors predict the survival in glioblastoma patients treated with postoperative chemoradiation therapy? *Acta Radiol* 2013;54:214–20.
- Pope WB, Mirsadraei L, Lai A, Eskin A, Qiao J, Kim HJ, et al. Differential gene expression in glioblastoma defined by ADC histogram analysis: relationship to extracellular matrix molecules and survival. *AJNR Am J Neuroradiol* 2012;33:1059–64.
- Saksena S, Jain R, Narang J, Scarpace L, Schultz LR, Lehman NL, et al. Predicting survival in glioblastomas using diffusion tensor imaging metrics. *J Magn Reson Imaging* 2010;32:788–95.
- Wedeen VJ, Hagmann P, Tseng WY, Reese TG, Weisskoff RM. Mapping complex tissue architecture with diffusion spectrum magnetic resonance imaging. *Magn Reson Med* 2005;54:1377–86.
- Tuch DS. Q-ball imaging. *Magn Reson Med* 2004;52:1358–72.
- Maier SE, Bogner P, Bajzik G, Mamata H, Mamata Y, Repa I, et al. Normal brain and brain tumor: multicomponent apparent diffusion coefficient line scan imaging. *Radiology* 2001;219:842–9.
- Mulkern RV, Gudbjartsson H, Westin CF, Zengingonul HP, Gartner W, Guttmann CR, et al. Multi-component apparent diffusion coefficients in human brain. *NMR Biomed* 1999;12:51–62.
- Bennett KM, Schminda KM, Bennett RT, Rowe DB, Lu H, Hyde JS. Characterization of continuously distributed cortical water diffusion rates with a stretched-exponential model. *Magn Reson Med* 2003;50:727–34.
- Jensen JH, Helpert JA, Ramani A, Lu H, Kaczynski K. Diffusional kurtosis imaging: the quantification of non-gaussian water diffusion by means of magnetic resonance imaging. *Magn Reson Med* 2005;53:1432–40.
- Le Bihan D, Breton E, Lallemand D, Grenier P, Cabanis E, Laval-Jeantet M. MR imaging of intravoxel incoherent motions: application to diffusion and perfusion in neurologic disorders. *Radiology* 1986;161:401–7.
- Merboldt K-D, Hanicke W, Frahm J. Self-diffusion NMR imaging using stimulated echoes. *J Magn Reson* 1985;64:479–86.
- Le Bihan D, Breton E. Imagerie de diffusion *in-vivo* par résonance. *C R Acad Sci* 1985;301:1109–12.
- Taylor DG, Bushell MC. The spatial mapping of translational diffusion coefficients by the NMR imaging technique. *Phys Med Biol* 1985;30:345–9.
- Stejskal EO, Tanner JE. Spin diffusion measurements: Spin echoes in the presence of a time-dependent field gradient. *J Chem Phys* 1965;42:288–92.
- Le Bihan D. Looking into the functional architecture of the brain with diffusion MRI. *Nat Rev Neurosci* 2003;4:469–80.
- Harris EJ, Burn GP. The transfer of sodium and potassium ions between muscle and the surrounding medium. *Trans Faraday Soc* 1949;45:508–28.
- Nicholson C. Diffusion and related transport mechanisms in brain tissue. *Rep Prog Phys* 2001;64:815.
- Sykova E, Nicholson C. Diffusion in brain extracellular space. *Physiol Rev* 2008;88:1277–340.
- Tao L, Nicholson C. Maximum geometrical hindrance to diffusion in brain extracellular space surrounding uniformly spaced convex cells. *J Theor Biol* 2004;229:59–68.
- Vargova L, Homola A, Zamecnik J, Tichy M, Benes V, Sykova E. Diffusion parameters of the extracellular space in human gliomas. *Glia* 2003;42:77–88.
- Le Bihan D. Molecular diffusion, tissue microdynamics and microstructure. *NMR Biomed* 1995;8:375–86.
- Stanisz GJ. Diffusion MR in biological systems: tissue compartments and exchange. *Isr J Chem* 2003;43:33–44.
- Tanner JE. Transient diffusion in a system partitioned by permeable barriers. Application to NMR measurements with a pulsed field gradient. *J Chem Phys* 1978;69:1748–54.
- Basser PJ, Mattiello J, LeBihan D. MR diffusion tensor spectroscopy and imaging. *Biophys J* 1994;66:259–67.
- Maier SE, Sun Y, Mulkern RV. Diffusion imaging of brain tumors. *NMR Biomed* 2010;23:849–64.

Grant Support

This study was supported by grants R01AG031224, R01EB000790, and RC2 DA29475 (A.M. Dale).

Received December 9, 2013; revised April 1, 2014; accepted May 19, 2014; published online September 2, 2014.

40. Chenevert TL, Sundgren PC, Ross BD. Diffusion imaging: insight to cell status and cytoarchitecture. *Neuroimaging Clin N Am* 2006;16: 619–32, viii–ix.
41. Nicholson C. Factors governing diffusing molecular signals in brain extracellular space. *J Neural Transm* 2005;112:29–44.
42. White NS, Dale AM. Distinct effects of nuclear volume fraction and cell diameter on high b-value diffusion MRI contrast in tumors. *Mag Res Med* 2013 Dec 19. [Epub ahead of print].
43. Gore JC, Xu J, Colvin DC, Yankeelov TE, Parsons EC, Does MD. Characterization of tissue structure at varying length scales using temporal diffusion spectroscopy. *NMR Biomed* 2010;23: 745–56.
44. Xu J, Li K, Smith RA, Waterton JC, Zhao P, Chen H, et al. Characterizing tumor response to chemotherapy at various length scales using temporal diffusion spectroscopy. *PLoS ONE* 2012;7:e41714.
45. White NS, Leergaard TB, D'Arceuil H, Bjaalie JG, Dale AM. Probing tissue microstructure with restriction spectrum imaging: histological and theoretical validation. *Hum Brain Mapp* 2013;34: 327–46.
46. White NS, Dale AM. Optimal diffusion MRI acquisition for fiber orientation density estimation: an analytic approach. *Hum Brain Mapp* 2009;30:3696–703.
47. White NS, McDonald CR, Farid N, Kuperman JM, Kesari S, Dale AM. Improved conspicuity and delineation of high-grade primary and metastatic brain tumors using "restriction spectrum imaging": quantitative comparison with high B-value DWI and ADC. *AJNR Am J Neuroradiol* 2013;34:958–64, S1.
48. White NS, Kuperman J, McDonald CR, Farid N, Kasai K, Shankaranarayanan A, et al. Restriction Spectrum Imaging of Glioblastoma Multiform: Comparison with ADC. In: *Proceedings of the 20th Annual Meeting ISMRM*; 2012; Melbourne, Australia.
49. Kothari PD, White NS, Farid N, Chung R, Kuperman JM, Girard HM, et al. Longitudinal restriction spectrum imaging is resistant to pseudoresponse in patients with high-grade gliomas treated with bevacizumab. *AJNR Am J Neuroradiol* 2013;34:1752–7.
50. McDonald CR, White NS, Farid N, Lai G, Kuperman JM, Bartsch H, et al. Recovery of white matter tracts in regions of peritumoral FLAIR hyperintensity with use of restriction spectrum imaging. *AJNR Am J Neuroradiol* 2013;34:1157–63.
51. Farid N, Almeida-Freitas DB, White NS, McDonald CR, Muller KA, Vandenberg SR, et al. Restriction-spectrum imaging of bevacizumab-related necrosis in a patient with GBM. *Front Oncol* 2013;3: 258.
52. Parsons EC, Does MD, Gore JC. Temporal diffusion spectroscopy: theory and implementation in restricted systems using oscillating gradients. *Magn Reson Med* 2006;55:75–84.
53. McNab JA, Edlow BL, Witzel T, Huang SY, Bhat H, Heberlein K, et al. The Human Connectome Project and beyond: initial applications of 300 mT/m gradients. *Neuroimage* 2013;80:234–45.
54. Castillo M, Smith JK, Kwok L, Wilber K. Apparent diffusion coefficients in the evaluation of high-grade cerebral gliomas. *Am J Neuroradiol* 2001;22:60–4.
55. Stadnik TW, Chaskis C, Michotte A, Shabana WM, van Rompaey K, Luytjaert R, et al. Diffusion-weighted MR imaging of intracerebral masses: comparison with conventional MR imaging and histologic findings. *Am J Neuroradiol* 2001;22:969–76.
56. Jain RK. Normalization of tumor vasculature: an emerging concept in antiangiogenic therapy. *Science* 2005;307:58–62.
57. Kamada K, Todo T, Masutani Y, Aoki S, Ino K, Takano T, et al. Combined use of tractography-integrated functional neuronavigation and direct fiber stimulation. *J Neurosurg* 2005;102:664–72.
58. Nimsky C, Ganslandt O, Hastreiter P, Wang R, Benner T, Sorensen AG, et al. Preoperative and intraoperative diffusion tensor imaging-based fiber tracking in glioma surgery. *Neurosurgery* 2005;56:130–7; discussion 8.
59. Mori S, Frederiksen K, van Zijl PC, Stieltjes B, Kraut MA, Solaiyappan M, et al. Brain white matter anatomy of tumor patients evaluated with diffusion tensor imaging. *Ann Neurol* 2002;51:377–80.
60. Yu CS, Li KC, Xuan Y, Ji XM, Qin W. Diffusion tensor tractography in patients with cerebral tumors: a helpful technique for neurosurgical planning and postoperative assessment. *Eur J Radiol* 2005;56: 197–204.
61. Kamada K, Houkin K, Takeuchi F, Ishii N, Ikeda J, Sawamura Y, et al. Visualization of the eloquent motor system by integration of MEG, functional, and anisotropic diffusion-weighted MRI in functional neuronavigation. *Surg Neurol* 2003;59:352–61.
62. Duffau H, Thiebaut de Schotten M, Mandonnet E. White matter functional connectivity as an additional landmark for dominant temporal lobectomy. *J Neurol Neurosurg Psychiatry* 2008;79: 492–5.
63. Nimsky C, Ganslandt O, von Keller B, Fahlbusch R. Preliminary experience in glioma surgery with intraoperative high-field MRI. *Acta Neurochir Suppl* 2003;88:21–9.
64. Nimsky C, Grummich P, Sorensen AG, Fahlbusch R, Ganslandt O. Visualization of the pyramidal tract in glioma surgery by integrating diffusion tensor imaging in functional neuronavigation. *Zentralbl Neurochir* 2005;66:133–41.
65. Sun GC, Chen XL, Zhao Y, Wang F, Hou BK, Wang YB, et al. Intraoperative high-field magnetic resonance imaging combined with fiber tract neuronavigation-guided resection of cerebral lesions involving optic radiation. *Neurosurgery* 2011;69:1070–84.
66. Bello L, Gambini A, Castellano A, Carrabba G, Acerbi F, Fava E, et al. Motor and language DTI fiber tracking combined with intraoperative subcortical mapping for surgical removal of gliomas. *Neuroimage* 2008;39:369–82.
67. Kinoshita M, Yamada K, Hashimoto N, Kato A, Izumoto S, Baba T, et al. Fiber-tracking does not accurately estimate size of fiber bundle in pathological condition: initial neurosurgical experience using neuronavigation and subcortical white matter stimulation. *Neuroimage* 2005;25:424–9.
68. Kesari S. Understanding glioblastoma tumor biology: the potential to improve current diagnosis and treatments. *Semin Oncol* 2011;38 Suppl 4:S2–10.
69. Mong S, Ellingson BM, Nghiemphu PL, Kim HJ, Mirsadraei L, Lai A, et al. Persistent diffusion-restricted lesions in bevacizumab-treated malignant gliomas are associated with improved survival compared with matched controls. *AJNR Am J Neuroradiol* 2012; 33:1763–70.
70. Jeyaretna DS, Curry WT Jr, Batchelor TT, Stemmer-Rachamimov A, Plotkin SR. Exacerbation of cerebral radiation necrosis by bevacizumab. *J Clin Oncol* 2011;29:e159–62.
71. Rieger J, Bahr O, Muller K, Franz K, Steinbach J, Hattingen E. Bevacizumab-induced diffusion-restricted lesions in malignant glioma patients. *J Neurooncol* 2010;99:49–56.
72. Kirkham AP, Emberton M, Allen C. How good is MRI at detecting and characterising cancer within the prostate? *Eur Urol* 2006;50:1163–74.
73. Bonekamp D, Macura KJ. Dynamic contrast-enhanced magnetic resonance imaging in the evaluation of the prostate. *Top Magn Reson Imaging* 2008;19:273–84.
74. Kurhanewicz J, Vigneron DB, Hricak H, Narayan P, Carroll P, Nelson SJ. Three-dimensional H-1 MR spectroscopic imaging of the *in situ* human prostate with high (0.24–0.7-cm³) spatial resolution. *Radiology* 1996;198:795–805.
75. Weinreb JC, Blume JD, Coakley FV, Wheeler TM, Cormack JB, Sotito CK, et al. Prostate cancer: sextant localization at MR imaging and MR spectroscopic imaging before prostatectomy—results of ACRIN prospective multi-institutional clinicopathologic study. *Radiology* 2009; 251:122–33.
76. Yoshimitsu K, Kiyoshima K, Irie H, Tajima T, Asayama Y, Hirakawa M, et al. Usefulness of apparent diffusion coefficient map in diagnosing prostate carcinoma: correlation with stepwise histopathology. *J Magn Reson Imaging* 2008;27:132–9.
77. Langer DL, van der Kwast TH, Evans AJ, Plotkin A, Trachtenberg J, Wilson BC, et al. Prostate tissue composition and MR measurements: investigating the relationships between ADC, T2, K(trans), v(e), and corresponding histologic features. *Radiology* 2010;255: 485–94.
78. Jezzard P, Balaban RS. Correction for geometric distortion in echo planar images from B₀ field variations. *Magn Reson Med* 1995;34: 65–73.

79. Andersson JLR, Skare S, Ashburner J. How to correct susceptibility distortions in spin-echo echo-planar images: application to diffusion tensor imaging. *Neuroimage* 2003;20:870–88.
80. Robson MD, Gore JC, Constable RT. Measurement of the point spread function in MRI using constant time imaging. *Magn Reson Med* 1997;38:733–40.
81. Holland D, Kuperman JM, Dale AM. Efficient correction of inhomogeneous static magnetic field-induced distortion in Echo Planar Imaging. *Neuroimage* 2010;50:175–83.
82. Morgan PS, Bowtell RW, McIntyre DJO, Worthington BS. Correction of spatial distortion in EPI due to inhomogeneous static magnetic fields using the reversed gradient method. *J Magn Reson Imaging* 2004;19:499–507.
83. Chang H, Fitzpatrick JM. A technique for accurate magnetic resonance imaging in the presence of field inhomogeneities. *IEEE Trans Med Imaging* 1992;11:319–29.
84. Gerstner ER, Sorensen AG. Diffusion and diffusion tensor imaging in brain cancer. *Semin Radiat Oncol* 2011;21:141–6.

Novel Technique for Characterizing Prostate Cancer Utilizing MRI Restriction Spectrum Imaging: Proof of Principle and Initial Clinical Experience with Extra-Prostatic Extension

Rebecca A. Rakow-Penner, MD, PhD¹, Nathan S. White, PhD¹, J. Kellogg Parsons, MD, MHS², Hyung W. Choi, MD¹, Michael A. Liss, MD², Joshua M. Kuperman, PhD¹, Natalie Schenker-Ahmed, PhD¹, Hauke Bartsch, PhD¹, Robert F. Mattrey, MD¹, William G. Bradley, MD, PhD¹, Ahmed Shabaik, MD³, Jiaoti Huang, MD⁴, Daniel J. A. Margolis, MD⁵, Steven S. Raman, MD⁵, Leonard Marks, MD⁶, Christopher J. Kane, MD², Robert E. Reiter, MD⁶, David S. Karow, MD, PhD¹, Anders M. Dale, PhD¹

Running title: Restriction Spectrum Imaging in the Prostate

Submitted to Prostate Cancer Prostatic Diseases, July 2014
Revision submitted October, 2014

Institutions:

¹Department of Radiology, University of California San Diego School of Medicine

²Department of Urology, University of California San Diego School of Medicine

³Department of Pathology, University of California San Diego School of Medicine

⁴Department of Pathology, University of California Los Angeles Geffen School of Medicine

⁵Department of Radiology, University of California Los Angeles Geffen School of Medicine

⁶Department of Urology, University of California Los Angeles Geffen School of Medicine

Corresponding Author:

David Karow

Multimodal Imaging Laboratory

8950 Villa La Jolla Drive Suite C101

La Jolla, CA 92037

Fax: (858)534-1078

Email: dskarow@ucsd.edu

Phone number: (858)534-1078

Key Words:

prostate diffusion imaging, extraprostatic extension, extracapsular extension, prostate MRI

Funding:

ACS-IRG (American Cancer Soc-Institutional Research Grant) #70-002

UCSD Clinician Scientist Program

No conflicts of interests.

Abstract

Background: Standard magnetic resonance imaging (MRI) of the prostate lacks sensitivity in the diagnosis and staging of prostate cancer (PCa). To improve the operating characteristics of prostate MRI in the detection and characterization of PCa, we developed a novel, enhanced MRI diffusion technique using restriction spectrum imaging (RSI-MRI).

Methods: We compared the efficacy of our novel RSI-MRI technique to standard MRI for detecting extra-prostatic extension in 7 PCa patients with histologically proven pT3a disease from a total of 28 PCa patients imaged. All 28 patients underwent MRI and RSI-MRI prior to radical prostatectomy.

Results: Pre-operative standard MRI correctly identified extra-prostatic extension in 2 of 7 (29%) patients, while RSI-MRI identified extra-prostatic extension in 7 of 7 (100%) patients.

Conclusions: We conclude that our novel RSI-MRI technology shows promise for substantially improving PCa imaging. Further translational studies of prostate RSI-MRI in the diagnosis and staging of prostate cancer are indicated.

Introduction

Multiparametric magnetic resonance imaging (MRI) is an emerging diagnostic tool for the screening, staging, and treatment of prostate cancer (PCa). (1-17) However, prostate MRI demonstrates variable sensitivity (49 – 88%) and specificity (84– 89%), which currently limits its clinical utility(2,3,14).

Standard diffusion weighted imaging (DWI) improves the operating characteristics of prostate MRI (2,3,14,16,18,19). DWI detects the diffusivity of microscopic water and subsequently reflects the cellularity and integrity of cells imaged. When combined with T2 weighted imaging and dynamic contrast enhanced imaging, DWI improves sensitivity and specificity of PCa diagnosis by increasing tumor conspicuity(2,14,16,18,19).

DWI also suffers from distortion due to magnetic field inhomogeneity (20) and relatively high false positive rates owing to hemorrhage (i.e. from prior biopsy), inflammatory processes, and benign nodules in the transitional zone (21). In order to overcome these challenges and improve magnetic resonance detection of PCa, we have developed a novel, sophisticated diffusion method termed prostate Restriction Spectrum Imaging (RSI), or RSI-MRI (22,23). By collecting a broader, more extended spectrum of diffusion images(22), combined with sophisticated modeling of differential water compartments in tissue and correction of spatial distortion(24), RSI-MRI theoretically focuses on the signal emanating from the intracellular water compartment of tumor cells and thereby minimizes false positive signals(25). A similar RSI technique,

recently applied to brain imaging, enhanced the signal of glioblastoma multiforme tumors by 10-fold (23).

In this pilot clinical study, we determined the clinical utility of our novel prostate RSI-MRI technique to stage PCa by assessing the accuracy of RSI-MRI to detect extra-prostatic extension (EPE) of tumor.

Materials and Methods

RSI-MRI

In this IRB approved prospective study, 28 enrolled patients underwent standard T2, perfusion (with Gadolinium) and diffusion protocols at 3T (Siemens, Erlangen Germany) with an endorectal coil (Table 1). The 28 patients had biopsy proven prostate cancer and an MRI was being performed for pre-surgical planning. The restriction spectrum protocol parameters included b-values 0, 800, 1500, 4000 s/mm² in 30 unique diffusion directions for each nonzero b-value. RSI cellularity maps isolating the restricted isotropic water fraction²³ were reconstructed based on all b-values and then standardized across the sample with z-score maps. The z-score maps were calculated by (1) measuring the mean and standard deviation of normal prostate signal from the raw RSI cellularity maps across the patient pool, (2) subtracting this measured mean value from each subjects RSI cellularity map (3) and dividing by the measured normal prostate standard deviation. Correction of image distortions in RSI maps due to B0 field inhomogeneities was performed using the alternating phase-encode technique(24). Per standard clinical protocol, radiology reports were generated by an experienced radiologist for each of the patients blinded to the RSI results (Table 2).

Correlation of RSI-MRI with histopathology

Whole mount histopathology was performed on the 28 enrolled patients who underwent RSI-MRI and subsequent radical prostatectomy. For the 8 radical prostatectomy patients with histologically identified EPE (pT3a disease), presurgical pelvic RSI-MRI imaging was reviewed. Out of the 8 patients with histologically identified EPE, one patient was excluded due to an error in data collection for the MRI-RSI, where distortion correction was unable to be performed. Thus, a total of 7 patients were used for evaluation in this pilot study.

The area of tumor was identified by an experienced uropathologist (Table 3). Clinical images were reviewed in a non-blinded fashion to verify performance of RSI-MRI (Figure 1), where pathology was available for comparison. Standard MRI (including T2, perfusion, and traditional DWI), RSI-MRI, and histopathology were compared at a multidisciplinary tumor board consisting of radiologists, urologists, and uropathologists. RSI-MRI images were reviewed to determine if the RSI signal extended beyond the prostatic capsule, defined as the T2 hypointense thin line separating parenchymal tissue from extraprostatic fat and neurovascular structures. RSI maps were spatially corrected and overlaid on standard T2 maps to determine if the RSI signal was intracapsular or bulging, blurring, or grossly extending beyond the capsule. This evaluation was then compared to the preoperative MRI Radiology reports to determine if EPE was suspected without RSI-MRI.

Results

Standard MRI

Using the standard preoperative MR protocol (T1 perfusion, T2, and basic diffusion-weighting), patients 1 and 5 demonstrated radiologic findings consistent with capsular involvement and EPE. Patient 4's imaging findings were suspicious for EPE but not definitive. Patients 3, 6, and 7 demonstrated standard MR radiologic findings consistent with bulging of the capsule, but no indication of EPE. Patient 2's standard imaging did not indicate concern for pathology abutting the capsule.

RSI-MRI

On analysis of RSI-MRI, 7 of 7 (100%) demonstrated EPE (Figure 1, column 4). The areas of EPE correlated with the areas encircled on the whole mount histopathology. Four of 7 (60%) patients with RSI-MRI detected EPE also had positive surgical margins. Figure 2 demonstrates 3 patients, out of the total 28 patients in the study, who did not demonstrate EPE.

RSI-MRI and Gleason grading

As a proof of principle in this small sample of patients, regions of interest were drawn over the areas of the tumor on the ADC maps and the RSI-MRI z-score maps to give representative mean values (Table 4). By convention, lower ADCs correlate to higher-grade tumors.

Discussion

In this pilot clinical study, we demonstrate the potential for our novel prostate RSI-MRI technique to substantially improve upon current imaging-based modalities for the diagnosis and staging of PCa. In our series, RSI-MRI successfully identified pT3a disease in 7 (100%) of 7

patients, while standard MRI accurately identified only 2 (29%) of 7. These data justify further translational studies of RSI-MRI for prostate cancer detection and staging.

RSI-MRI's sensitivity to intracellular diffusivity differentiates it from standard DWI(22). Extracellular signal emanating from surrounding inflammatory processes and hemorrhage contribute less to the signal detected by RSI-MRI as compared to standard DWI. RSI-MRI minimizes these effects by focusing on the signal emanating from intracellular tumor cells (restricted diffusion within small spherical compartments), with less focus on the extracellular signal (hindered and free water diffusion). RSI-MRI achieves this by collecting diffusion images over an extended b-value range ($b = 0$ to 4000 s/mm^2) and decomposing the relative contribution from separable water compartments within voxels using a linear mixture model framework (22,23). Standard quantitative diffusion techniques acquire data with b-values less than $1,000 \text{ s/mm}^2$. In addition, unlike conventional diffusion imaging and ADC maps, RSI-MRI maps are distortion-corrected and directly overlayed on T2 anatomic images with voxel specific accuracy, permitting more accurate assessment of signal beyond the capsular border. This increases the conspicuity of the extraprostatic extension.

Current standard MRI prostate protocols lack accurate localization of prostate cancer. RSI-MRI notably improves tumor localization with MRI, potentially rendering MR imaging more relevant in a variety of clinical scenarios. Pre-surgical MRI results may provide additional information for clinicians and patients by informing surgical planning (i.e. nerve-sparing). Other potential applications for RSI-MRI meriting further study include lesion localization for targeting of

image-guided biopsies, serial imaging in an active surveillance population, and evaluation of post-treatment recurrence following primary radiotherapy.

A challenge in further developing clinical applications of RSI-MRI lies in accurately defining its specificity, sensitivity, and positive and negative predictive values. Limitations of this current study included the small number of patients, and the retrospective non-blinded nature of the study. This was necessary for this pilot study for innovative methodological development, but suffers due to potential reader bias. An ongoing, blinded prospective study will allow for more detailed evaluations of the operating characteristics of RSI-MRI relative to standard MRI. RSI-MRI is a standardized quantitative technique and can potentially be employed across platforms and institutions. The color bar in Figure 1 illustrates the z-score scale for the RSI maps. As the number of enrollees increase, the z-score threshold range for concern for malignancy can be determined by pooling the variance across patients. One of the challenges of standard diffusion imaging, is that the ADC values are not standardized across MRI scanners. The z-score is a standardized statistical method and inherently normalizes across the patient pool. Thus, the z-score is a value that can be compared across different scanners and provides a more robust value for relative comparison.

In summary, in this proof of concept study, we present our initial clinical experience with prostate RSI-MRI. RSI-MRI has the potential to substantially improve the radiological detection and characterization of PCa. Further translational studies will focus on defining its operating characteristics with respect to diagnosis and staging.

Acknowledgments: The authors would like to thank Brenda Brown for her help on this project.

Conflicts of interest: The authors do not have any conflicts of interest.

Funding:

This work was supported by the Department of Defense, Prostate Cancer Research Program

W81XWH-13-1-0391, and the American Cancer Society – Institutional Research Grant #70-002.

References

1. Turkbey B, Pinto PA, Mani H, Bernardo M, Pang Y, McKinney YL, et al. Prostate cancer: value of multiparametric MR imaging at 3 T for detection--histopathologic correlation. *Radiology* 2010; 255: 89–99.
2. Isebaert S, Van den Bergh L, Haustermans K, Joniau S, Lerut E, De Wever L, et al. Multiparametric MRI for prostate cancer localization in correlation to whole-mount histopathology. *J Magn Reson Imaging* 2013; 37: 1392–1401.
3. Haider MA, van der Kwast TH, Tanguay J, Evans AJ, Hashmi A-T, Lockwood G, et al. Combined T2-weighted and diffusion-weighted MRI for localization of prostate cancer. *AJR American journal of roentgenology* 2007; 189: 323–328.
4. Rastinehad AR, Baccala AA, Chung PH, Proano JM, Kruecker J, Xu S, et al. D'Amico risk stratification correlates with degree of suspicion of prostate cancer on multiparametric magnetic resonance imaging. *J Urol* 2011; 185: 815–820.
5. Rais-Bahrami S, TürkbeY B, Rastinehad AR, Walton-Diaz A, Hoang AN, Siddiqui MM, et al. Natural history of small index lesions suspicious for prostate cancer on multiparametric MRI: recommendations for interval imaging follow-up. *Diagn Interv Radiol* 2014; e-pub ahead of print 30 April 2014; doi:10.5152/dir.2014.13319.
6. Abd-Alazeez M, Ahmed HU, Arya M, Charman SC, Anastasiadis E, Freeman A, et al. The accuracy of multiparametric MRI in men with negative biopsy and elevated PSA level--can it rule out clinically significant prostate cancer? *Urol Oncol* 2014; 32 :45.e17–22.
7. Hoeks CMA, Somford DM, van Oort IM, Vergunst H, Oddens JR, Smits GA, et al. Value of 3-T multiparametric magnetic resonance imaging and magnetic resonance-guided biopsy for early risk restratification in active surveillance of low-risk prostate cancer: a prospective multicenter cohort study. *Investigative radiology* 2014; 49: 165–172.

8. Stamatakis L, Siddiqui MM, Nix JW, Logan J, Rais-Bahrami S, Walton-Diaz A, et al. Accuracy of multiparametric magnetic resonance imaging in confirming eligibility for active surveillance for men with prostate cancer. *Cancer* 2013; 119: 3359–3366.
9. Abd-Alazeez M, Kirkham A, Ahmed HU, Arya M, Anastasiadis E, Charman SC, et al. Performance of multiparametric MRI in men at risk of prostate cancer before the first biopsy: a paired validating cohort study using template prostate mapping biopsies as the reference standard. *Prostate Cancer Prostatic Dis* 2014; 17: 40–46.
10. Turkbey B, Mani H, Aras O, Ho J, Hoang A, Rastinehad AR, et al. Prostate Cancer: Can Multiparametric MR Imaging Help Identify Patients Who Are Candidates for Active Surveillance? *Radiology* 2013; 268:144–152.
11. Rais-Bahrami S, Siddiqui MM, Turkbey B, Stamatakis L, Logan J, Hoang AN, et al. Utility of Multiparametric Magnetic Resonance Imaging Suspicion Levels for Detecting Prostate Cancer. *J Urol* 2013; 190: 1721–1727.
12. Park JJ, Kim CK, Park SY, Park BK, Lee HM, Cho SW. Prostate Cancer: Role of Pretreatment Multiparametric 3-T MRI in Predicting Biochemical Recurrence After Radical Prostatectomy. *Am J Radiol*; 2014; 202: W459–65.
13. Somford DM, Hamoen EH, Fütterer JJ, van Basten JP, Hulsbergen-van de Kaa CA, Vreuls W, et al. The predictive value of endorectal 3 Tesla multiparametric magnetic resonance imaging for extraprostatic extension in patients with low, intermediate and high risk prostate cancer. *J Urol* 2013; 190: 1728–1734.
14. Lim HK, Kim JK, Kim KA, Cho K-S. Prostate cancer: apparent diffusion coefficient map with T2-weighted images for detection--a multireader study. *Radiology* 2009; 250: 145–151.
15. Tanimoto A, Nakashima J, Kohno H, Shinmoto H, Kuribayashi S. Prostate cancer screening: the clinical value of diffusion-weighted imaging and dynamic MR imaging in combination with T2-weighted imaging. *J Magn Reson Imaging* 2007; 25: 146–152.
16. Donati OF, Jung SI, Vargas HA, Gultekin DH, Zheng J, Moskowitz CS, et al. Multiparametric prostate MR imaging with T2-weighted, diffusion-weighted, and dynamic contrast-enhanced sequences: are all pulse sequences necessary to detect locally recurrent prostate cancer after radiation therapy? *Radiology* 2013; 268: 440–450.
17. Mazaheri Y, Hricak H, Fine SW, Akin O, Shukla-Dave A, Ishill NM, et al. Prostate tumor volume measurement with combined T2-weighted imaging and diffusion-weighted MR: correlation with pathologic tumor volume. *Radiology* 2009; 252: 449–457.
18. Miao H, Fukatsu H, Ishigaki T. Prostate cancer detection with 3-T MRI: comparison of diffusion-weighted and T2-weighted imaging. *Eur J Radiol* 2007; 61: 297–302.
19. Giannarini G, Nguyen DP, Thalmann GN, Thoeny HC. Diffusion-weighted magnetic resonance imaging detects local recurrence after radical prostatectomy: initial experience.

Eur Urol 2012; 61: 616–620.

20. Donato F, Costa DN, Yuan Q, Rofsky NM, Lenkinski RE, Pedrosa I. Geometric Distortion in Diffusion-weighted MR Imaging of the Prostate-Contributing Factors and Strategies for Improvement. *Acad Radiol* 2014; 21: 817–823.
21. Yoshimitsu K, Kiyoshima K, Irie H, Tajima T, Asayama Y, Hirakawa M, et al. Usefulness of apparent diffusion coefficient map in diagnosing prostate carcinoma: correlation with stepwise histopathology. *J Magn Reson Imaging* 2008; 27: 132–139.
22. White NS, Leergaard TB, D'Arceuil H, Bjaalie JG, Dale AM. Probing tissue microstructure with restriction spectrum imaging: Histological and theoretical validation. *Hum Brain Mapp* 2013; 34: 327–346.
23. White NS, McDonald CR, Farid N, Kuperman JM, Kesari S, Dale AM. Improved Conspicuity and Delineation of High-Grade Primary and Metastatic Brain Tumors Using “Restriction Spectrum Imaging”: Quantitative Comparison with High B-Value DWI and ADC. *Am J Neuroradiol* 2012; 34: 958-964.
24. Holland D, Kuperman JM, Dale AM. Efficient correction of inhomogeneous static magnetic field-induced distortion in Echo Planar Imaging. *Neuroimage* 2010; 50: 175–183.
25. White NS, Dale AM. Distinct effects of nuclear volume fraction and cell diameter on high b-value diffusion MRI contrast in tumors. *Magn Reson Med* 2013; e-pub ahead of print 19 December 2013, doi:10.1002/mrm.25039.

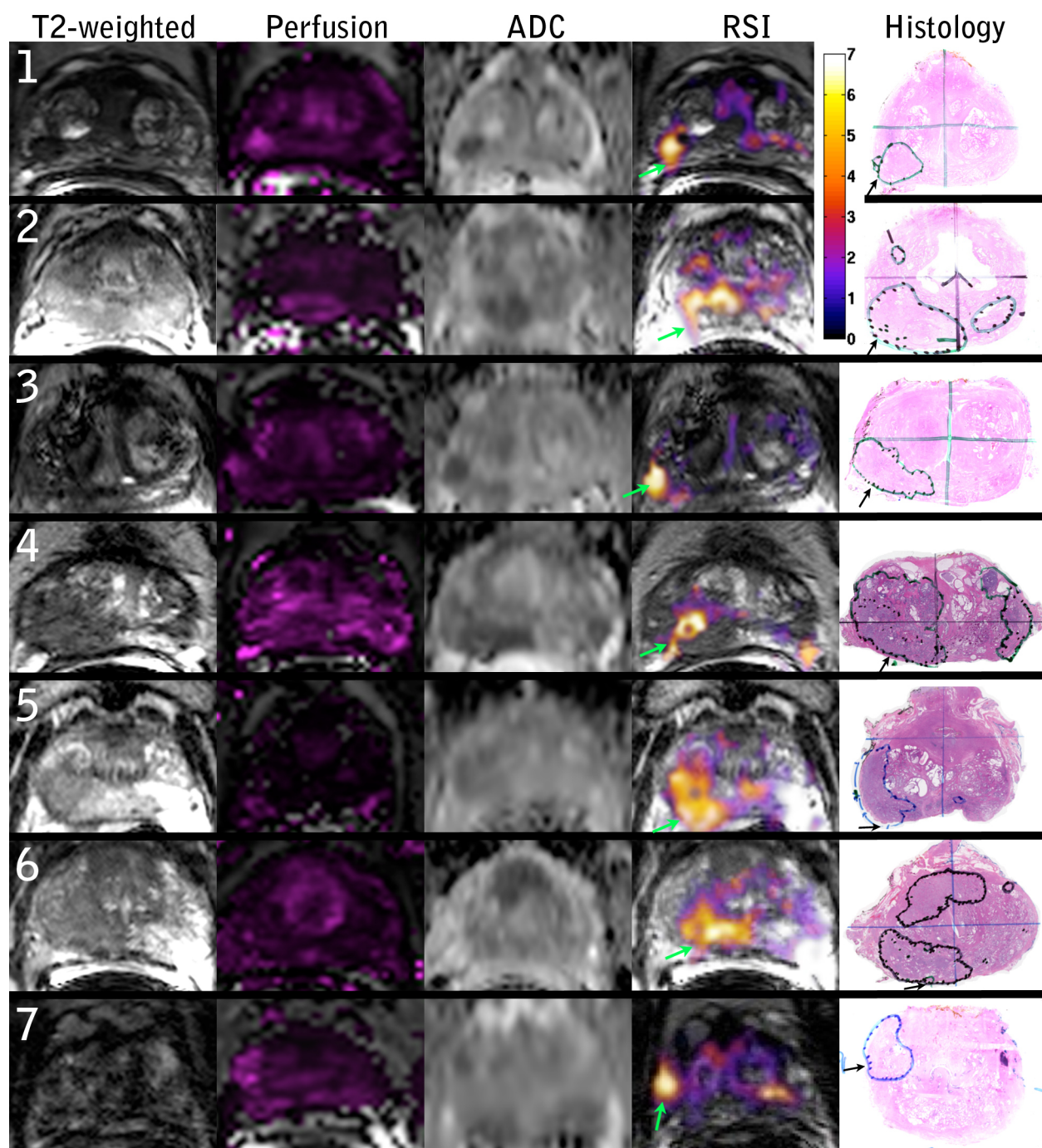


Figure 1. MR imaging and whole mount pathology for 7 prostate cancer patients with EPE. Column 1: T2 – weighted images, column 2: Perfusion K_{trans} maps, column 3: standard apparent diffusion coefficient (ADC) maps ($b = 0, 100, 400, \text{ and } 800 \text{ s/mm}^2$), column 4: RSI z-score maps, column 5: whole mount pathology with tumor and area of EPE identified. Color bar represents zscores from 0 to 7 for the RSI maps.

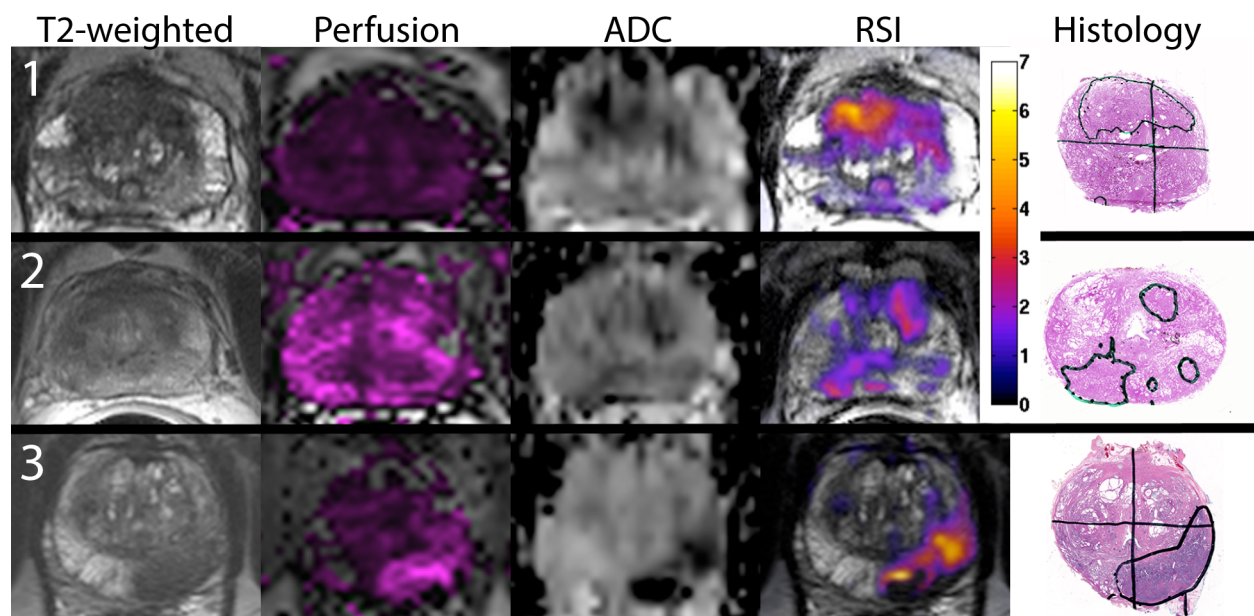


Figure 2. MR imaging and whole mount pathology for 3 prostate cancer patients without EPE. Column 1: T2 – weighted images, column 2: Perfusion K_{trans} maps, column 3: standard apparent diffusion coefficient (ADC) maps ($b = 0, 100, 400, \text{ and } 800 \text{ s/mm}^2$), column 4: RSI z-score maps, column 5: whole mount pathology with tumor and area of EPE identified. Color bar represents zscores from 0 to 7 for the RSI maps.

Table 1. MRI scan parameters for prostate MRI protocol at 3T	
Pulse sequence	Parameters
T2	Axial 3D TSE T2 (Siemens SPACE, TR/TE 3800-5040/101 ETL 13, 14 cm FOV, 256 x 256 matrix, 1.5 mm contiguous slices)
Diffusion-weighted (Standard)	(echoplanar, TR/TE 3900/60, 21 x 26 cm FOV, 130 x 160 matrix, 3.6 mm slices, 4 NEX, b-values 0, 100, 400, 800 s/mm ²)
T1 Dynamic Perfusion Imaging	(Siemens TWIST, TR./TE 3.9/1.4 ms, 12° flip angle, 26 x 26 cm FOV, 160 x 160 matrix, 3.6 mm slices, 4.75 s/acquisition over 6 minutes with 15 s injection delay, image analysis using iCAD Versavue)
Restriction Spectrum Imaging	Spin echo EPI, TR/TE 5500/137, 26 x 26 cm FOV, 128 x 96 matrix, 3.6 mm slices, 30 directions at each b-value, b-values 0, 800, 1500, 4000 s/mm ² .

Table 2. Radiologic findings – documented diagnostic interpretations Din 7 patients with biopsy-proven localized prostate cancer				
Case	Location	Axial Clock Face Location	Capsular Involvement	Technical Quality
1	Right peripheral gland	7 – 8 o'clock	Focal EPE may involve adjacent right neurovascular bundle. Right seminal vesicle invasion.	Excellent, no limitations
2	Right central peripheral basal mid gland	7 o'clock	Intact, no suspicion for involvement	Excellent, no limitations
3	Right peripheral basal mid gland	8 o'clock	Bulges the capsule with a broad base of contact, organ confined disease	Excellent, no limitations
4	Right peripheral gland lesion	6 – 9 o'clock	Bulges the capsule, suspicious but not definitive for extracapsular extension	Excellent, no limitations
5	R peripheral gland from apex to base	5-10 o' clock	Blurring and irregularity of right capsule, suspicious for capsular involvement	Limited spectral quality, does not diminish diagnostic confidence
6	R peripheral base lesion	7 o' clock	Bulges the capsule with a broad base of attachment	Excellent, no limitations
7	Right peripheral mid gland	9 – 10 o'clock	Bulges the capsule laterally	Hemorrhage limits sensitivity and functional characterization

Table 3. Pathologic findings determined from post resection whole mount pathology in 7 patients undergoing radical prostatectomy

Case	Gleason	Location of EPE	Staging	Age	PSA	Surgical Margins at Site of EPE
1	3 + 4	Right Posterior	pT3bNxMx	61	5.8	Negative
2	3 + 4	Right Posterior	pT3aN0Mx	55	2.7	Positive
3	4 + 5	Right Posterior	pT3bpN1Mx	64	8.2	Negative
4	4 + 3	Right Posterior	pT3aN1Mx	64	4.2	Positive
5	4 + 5	Right Posterior	pT3aN1Mx	68	7	Positive
6	4 + 3	Right Posterior	pT3apN0Mx	56	10	Positive
7	4 + 3	Right Antero-lateral	pT3apN0Mx	67	5.1	Negative

Table 4. Quantitative Diffusion Imaging – range of ADC scores and corresponding RSI Z-scores

Case	ADC ($10^{-3} \text{ mm}^2/\text{s}$)	RSI Z-score
1	1.08	5.9
2	0.99	5.7
3	1.01	5.8
4	0.89	4.6
5	1.26	6.6
6	1.38	4.2
7	1.12	5.0

MRI-derived Restriction Spectrum Imaging Cellularity Index is Associated with High Grade Prostate Cancer on Radical Prostatectomy Specimens

Michael A. Liss, MD, MAS^{1*}, Nathan S. White, PhD², J. Kellogg Parsons, MD, MHS¹, Natalie M. Schenker-Ahmed, PhD², Rebecca Rakow-Penner, MD, PhD², Joshua M. Kuperman, PhD², Hauke Bartsch, PhD², Hyung W. Choi², William G. Bradley, MD, PhD², Ahmed Shabaik, MD³, Jiaoti Huang, MD⁴, Daniel J. A. Margolis, MD⁵, Steven S. Raman, MD⁵, Leonard Marks, MD⁵, Christopher J. Kane, MD¹, Robert E. Reiter, MD⁶, Anders M. Dale, PhD^{2,6}, David S. Karow, MD, PhD²

1. Department of Urology, University of California San Diego School of Medicine

2. Department of Radiology, University of California San Diego School of Medicine

3. Department of Pathology, University of California San Diego School of Medicine

3. Department of Pathology, University of California Los Angeles Geffen School of Medicine

4. Department of Radiology, University of California Los Angeles Geffen School of Medicine

5. Department of Urology, University of California Los Angeles Geffen School of Medicine

6. Department of Neurosciences, University of California San Diego, La Jolla, CA

Corresponding Author:

Michael A. Liss MD

UCSD Moores Cancer Center

3855 Health Sciences Drive

La Jolla, Ca 92093, MC 0987

Office: (858) 822-7874

Fax: (858) 822-6188

Email: mliss008@gmail.com

Conflicts of Interest: None

Funding: DoD, Prostate Cancer Research Program, Idea Development Award

W81XWH-13-1-0391, #PC120532, ACS-IRG (American Cancer Society-

Institutional Research Grant) #70-002, and UCSD Clinician Scientist Program

Abstract

Purpose: We evaluate a novel magnetic resonance imaging (MRI) technique to improve detection of aggressive prostate cancer.

Materials and Methods: We performed a retrospective analysis of presurgical prostate MRI scans using an advanced diffusion weighted imaging technique called Restriction Spectrum Imaging (RSI), which can be presented as a normalized z-score statistic. Scans were acquired prior to radical prostatectomy. Prostatectomy specimens were processed using whole mount sectioning and regions of interest (ROIs) were drawn around individual prostate cancer (PCa) tumors. Corresponding ROIs were drawn on the MRI imaging and paired with ROIs in regions with no pathology. RSI z-score and conventional apparent diffusion coefficient (ADC) values were recorded for each ROI. Paired t-test, ANOVA and logistic regression analyses were performed.

Results: We evaluated 28 patients with 64 regions of interest (28 benign and 36 PCa). The mean difference in RSI z-score (PCa ROI – Benign ROI) was 2.17 (SE = 0.11; $p < 0.001$) and in ADC was 551 mm²/sec (SE = 80 mm²/sec; paired t-test, $p < 0.001$). The differences in the means among all groups (benign, primary Gleason 3 and primary Gleason 4) was significant for both RSI z-score ($F_{3,64} = 97.7$, $p < 0.001$) and ADC ($F_{3,64} = 13.9$, $p < 0.001$). A t-test was performed on only PCa tumor ROIs (n=36) to determine prostate cancer aggressiveness (Gleason 3 vs. Gleason 4) revealing that RSI z-score was still significant ($p = 0.03$), whereas, ADC values were no longer significant ($p = 0.08$). In multivariable analysis

adjusting for age and race, RSI z-score was associated with PCa aggressiveness (OR 10.3, 95%CI: 1.4-78.0, $p=0.02$) while ADC trended to significance ($p=0.07$).

Conclusions: The RSI derived normalized cellularity index (RSI z-score) is associated with aggressive prostate cancer as determined by pathologic Gleason scores. Further utilization of RSI techniques may serve to enhance standardized reporting systems for PCa in the future.

Introduction

One current focus in prostate cancer (PCa) diagnosis is to distinguish indolent from more aggressive disease to reduce over-treatment.^{1, 2} Magnetic resonance imaging (MRI) may be a non-invasive imaging biomarker to incorporate into PCa detection and treatment strategies.³

Recently, MRI has been increasingly investigated for use as a tool in the screening, staging, and monitoring of prostate cancer.⁴⁻⁶ Imaging techniques such as diffusion-weighted imaging (DWI) and the resultant quantitative apparent diffusion coefficient (ADC) have shown correlation with PCa; however, they have significant limitations regarding tumor conspicuity and localization.^{7, 8} A novel, advanced diffusion-based imaging technique, called Restriction Spectrum Imaging (RSI), has been modified from previous studies in brain cancer detection to apply to patients with prostate cancer.^{8, 9} Some benefits of the RSI technique is to provide reduced spatial distortion, enhanced tumor contrast-to-noise over conventional diffusion weighted imaging (DWI) and a normalized *in vivo* measure of cellularity.

Within individual tumor regions of interest, we investigate the association of final pathologic Gleason score from whole-mount prostatectomy specimens with the RSI cellularity index as compared to the current standard, ADC.¹⁰⁻¹⁶ Our primary outcome is the detection of primary pattern Gleason ≥ 4 prostate cancer.

Materials and Methods

Patients

All patients were previously diagnosed with prostate cancer via standard transrectal ultrasound guided prostate biopsy after prostate specific antigen (PSA) elevation or abnormal digital rectal examination (DRE). Pre-surgical pelvic MRI is routinely used at our institution to identify extraprostatic extension (EPE) in order to guide nerve-sparing surgery. Data were collected from chart review.

MRI and RSI

Patients underwent standard T2, perfusion (with Gadolinium) and diffusion protocols at 3T (Siemens, Erlangen Germany) with an endorectal coil prior to radical prostatectomy. Table 1 shows pulse sequence details. The ADC maps used to draw ROIs were generated from the low b-value, 800s/mm², derived from the same spectrum of b-values used in the RSI protocol. ADC maps were corrected for spatial distortion (ref 17). The restriction spectrum diffusion tensor imaging protocol parameters include b-values of 0, 800, 1500, 4000 s/mm² in 30 unique diffusion directions for each nonzero b-value. Imaging time for this sequence is approximately 3.5 minutes. RSI cellularity maps were reconstructed based on all b-values⁸. The RSI cellularity maps were then standardized across the sample, using the mean and standard deviations of normal prostate signal from the raw RSI maps in 20 patients to produce z-score maps. RSI maps were also corrected for spatial distortion.¹⁷

Pathology

After prostatectomy, whole mount histopathology was performed on 4 μm thick sections of each specimen. A Gleason score was assigned to each representative tumor location. If two tumors were located, the Gleason score for each was assessed independently. The histopathology was evaluated and the boundaries of tumor versus benign tissue were identified by a uropathologist.

Outcomes

We defined our primary outcome as pathologic primary Gleason score of 4, which means that Gleason 4 is the dominant histologic architecture and includes 4+3, 4+4, and 4+5 Gleason patterns. The pathologic Gleason score is currently the standard of reference for PCa aggressiveness. Additionally, the ability of imaging to detect secondary Gleason patterns may be minimal; therefore, herein we focus on primary Gleason patterns. Our primary predictor variable was the normalized cellularity index called the “RSI z-score”. The most commonly utilized tool to identify and classify aggressive cancer on MRI currently is the ADC value from DWI; therefore, the RSI z-score was compared with ADC to assess the predictive value in differentiating cancer from normal regions of interest (ROI).

Each patient had at least one identified region of cancerous tissue. If two areas of cancer were detected, each region was evaluated and assigned a separate Gleason score, ADC, and z-score. Tumor ROI's were drawn based on the

pathology in combination with ADC images that had been corrected for spatial distortion. A benign region of interest (ROI) was defined in a region of the prostate seen to be free of prostate cancer on the whole mount histology. ADC and RSI z-score values were recorded for all ROIs.

Statistical Analysis

Each patient had at least one ROI of cancer and one ROI of benign tissue. Correlation between the RSI-derived z-score and ADC was determined by a Pearson correlation test assuming normal distribution. In order to investigate the association of RSI z-score and primary Gleason pattern 4 PCa vs. pattern 3 PCa, a t-test test was performed. In order to compare the utility of MRI techniques (RSI z-score vs. ADC) for detecting aggressive cancer, we compared ROIs representing pathologically benign tissue with those representing increasing aggressive prostate cancer (benign vs. Gleason 3 vs. Gleason 4 primary patterns) using ANOVA analysis (F-test). After removing the values for the benign ROIs, we also assessed variation in MRI values among different grades of cancerous tissue aggressiveness by performing a comparative t-test. Multivariable analysis included an ordinal logistic regression (benign vs. Gleason 3 vs. Gleason 4) and binary logistic regression (Gleason 3 vs. Gleason 4). p-values less than 0.05 were considered statistically significant using the statistical package SPSS v.21 (IBM, Chicago, IL.).

Results

We identified 28 patients who underwent preoperative MRI with RSI and subsequent whole mount pathology after radical prostatectomy, with surgery taking place between May 2012 and May 2013. Demographics are displayed in Table 2. Figure 1 shows representative examples of RSI across the Gleason spectrum and illustrates data collection methods. White arrows within the higher grade RSI maps show areas of signal void that could be interpreted as false positives on the corresponding ADC maps. We identified 64 regions of interest (28 benign and 36 PCa). Eight patients had two distinct tumor ROIs within one specimen. Seven of those patients had discordant tumors (two different Gleason scores) and only one patient had two concordant tumor ROIs (both Gleason 3+4). The RSI z-score data for all ROIs, grouped by Gleason score, is shown in Figure 2.

ADC and RSI z-scores are normally distributed and did not need further transformation. There is a significant correlation between ADC and RSI z-score (Pearson $R = 0.69$; $n=64$, $p < 0.001$) (see supplementary figure). ADC and RSI z-score are collinear (collinearity index 8.4); therefore, they cannot be placed within the same multivariate analytic model.

The mean cellularity index (RSI z-score) in PCa was 2.53 (SE = 0.10) and in benign tissue 0.39 (SE = 0.12; $p < 0.001$). The mean ADC for PCa was 1169

mm²/sec (SE = 67 mm²/sec) and benign was 1679 mm²/sec (SE = 81 mm²/sec, p <0.001).

For the univariate and multivariate analyses, the data were grouped by primary Gleason pattern, either primary Gleason 3 (3+3 or 3+4) or Gleason 4 (4+3, 4+4, or 4+5). In univariable analysis, we investigate the association of RSI z-score and ADC with PCa on pathology (benign vs. Gleason 3 vs. Gleason 4) using ANOVA analysis. Both were able to distinguish benign from increasingly malignant prostate cancer (both p<0.001) (Table 3). Figure 3 displays a box-plot developed from individual ROI RSI z-scores corresponding to benign tissue primary Gleason 3 pattern or primary Gleason 4 pattern PCa tumors. When removing the benign regions of interest as to only compare low-grade (primary Gleason 3) to high-grade PCA (primary Gleason 4), RSI technique was able to distinguish the two groups (p=0.03) and ADC trended to significance (p=0.08). We then investigated these same parameters in multivariable analysis and determined that both RSI z-score and ADC were able to distinguish between the three groups in ordinal regression analysis adjusting for age and race (white vs. non-white); though the log odds of the parameter estimates suggest an improved distinction of the groups by RSI (RSI z-score and ADC, p<0.001). However, when determining the difference in the detection of low-grade and high-grade PCa, a higher RSI z-score was significantly associated with the higher-grade primary Gleason 4 pattern (Odds ratio 10.3 (1.4-78.0; p=0.02) and ADC showed a trend in distinguishing between the two Gleason patterns (p=0.07) (Table 4).

Discussion

Magnetic Resonance Restriction Spectrum Imaging normalized cellularity index (RSI z-score) is able to distinguish aggressive PCa (primary Gleason score of 4 compared to 3) in our population of men undergoing radical prostatectomy. Importantly, the RSI technique has displayed at least similar ability to distinguish Gleason grade to the current reference standard, ADC values.

Multiple studies have described the ability of ADC to detect PCa. However, the distinction between prostate cancer aggressiveness has been less investigated. Donati et al. found that mean ADC could distinguish Gleason 6 from 7+ tumors in 131 men undergoing prostatectomy (AUC 0.706) and in another paper discussed the use of 10th percentile ADC correlation to aggressiveness.^{10, 16} The 10th percentile ACD was also used in combination with mean ADC, T2-weighted skewness and k trans to distinguish PCa using computer aided diagnosis.¹⁸ Moreover, a recent study has suggested that ADC entropy rather than mean ADC could better discriminate the proportion of Gleason 4 cancer among Gleason 3+4 and 4+3 tumors.¹⁹ The distinction in primary Gleason pattern may have significant clinical implications regarding prostate cancer management decision-making.

Primary Gleason 4 pattern is an aggressive cancer with patients experiencing higher rates of biochemical (PSA) failure after prostatectomy, systemic recurrence and PCa mortality.²⁰ Therefore, knowledge of high-grade cancer prior to making management decisions would be helpful in determining treatment strategy. For example, men without Gleason 4 pattern PCa are more ideal candidates for active surveillance.²² Serial imaging may indicate progression of disease, assisting urologists in deciding when a biopsy off of protocol is warranted. Additionally, PCa grade may influence the urologic surgeon to perform a pelvic lymph node dissection at the time of prostatectomy due to increased risk of nodal disease.²¹

Currently, ADC serves as the most discriminatory parameter to assist radiologists for the detection of cancer. Moreover, recent examination of ADC and prostate cancer has shown the association of ADC and PCa aggressiveness.^{10, 16} While we do show that ADC can differentiate the presence of cancer or not, our study shows ADC is less able to determine the subtlety of primary pattern Gleason 3 vs. Gleason 4 PCa. Possible reasons include the proportion of pattern 3 vs. 4 disease in our population compared to prior populations, the b-values used in determining the ADC, how the ROI was chosen, the amount of stromal reaction, and technical factors such as degree of hemorrhage. The differences between ADC and RSI z-score in our study are small however.

RSI techniques offer advantages when compared to conventional DWI and ADC maps. For example, one of the challenges of standard diffusion imaging, is that the ADC values are not standardized across MRI scanners. The z-score is a standardized statistical method and inherently normalizes across the patient pool. Thus, the RSI z-score is a value that could potentially be compared across different scanners and institutions and provide a more robust value for relative comparison.

In addition, conventional DWI/ADC suffers from geometric distortion and can be difficult to interpret by clinicians and untrained radiologists. Distortion correction techniques previously optimized in the brain for GBM, are incorporated into our restriction spectrum imaging post-processing stream in order to derive spatially corrected cellularity maps. Distortion correction techniques are not routinely employed in conventional DWI and resultant ADC maps. Thus, the RSI maps can be co-registered with T2 weighted anatomic images with voxel accuracy. This has potential implications for more accurate detection of extraprostatic extension (ref Rebecca's accepted paper) and more accurate MRI-fused ultrasound targeted biopsy results.

Because of its greater sensitivity to restriction rather than hindered diffusion, RSI may be less subject to hemorrhage, inflammatory processes, and benign nodules in the transitional zone, all of which can exhibit lower ADC values leading to false positives. Theoretically, RSI-MRI reduces extracellular signal by focusing on the

signal emanating from intracellular tumor cells (restriction diffusion) and less from the extracellular signal (hindered diffusion).⁹ This will need to be rigorously tested in future ROC performance studies.

In addition, in regions where there is overt chemical dephasing from gross calcium or hemorrhage or other etiology, resulting in signal void, ADC maps will show these areas as low signal, which can be interpreted inaccurately, leading to a false positive. White arrow heads in Figure 1 show two such examples. For example, in the Gleason 5+4 case, the anterior region of signal void shows up as dark (low) on the ADC maps, potentially a false positive, while in the RSI maps, this is clearly interpreted as an area of signal void, not tumor. Thus, RSI offers a number of potential advantages when compared to DWI/ADC.

Certain limitations of this study include small sample size and retrospective data collection. We have overcome the small sample size by using each patient as his own control to provide a paired analysis by using known benign tissue. However, because of the small sample size we have fewer patients with extremely high-grade cancer (Gleason 5) and low-grade (Gleason 6 or less); therefore, we dichotomized based on the primary Gleason pattern. Additionally, we feel imaging is unlikely to visualize smaller amounts (secondary patterns) of PCa architecture. We do have a selection bias regarding our patient population as all patients underwent radical prostatectomy. Therefore, our results may not necessarily apply to patients in the general PSA screening population undergoing

prostate biopsy is an area of future investigation. The lack of patients in this study with pathologies at the extremes shows the need for a broader study.

Conclusions

Magnetic Resonance Restriction Spectrum Imaging, which can provide a normalized index of cellularity (RSI z-score), is associated with detection of aggressive PCa as defined by Gleason score. Additionally, RSI includes correction of spatial distortion, a normalized measure of cellularity and in general increased conspicuity when compared to conventional DWI/ADC. RSI technology warrants prospective evaluation in the PCa diagnostic arena.

References

1. Johansson, J. E., Andren, O., Andersson, S. O. et al.: Natural history of early, localized prostate cancer. *JAMA*, **291**: 2713, 2004
2. Loeb, S., Bjurlin, M. A., Nicholson, J. et al.: Overdiagnosis and overtreatment of prostate cancer. *Eur Urol*, **65**: 1046, 2014
3. van den Bergh, R. C., Ahmed, H. U., Bangma, C. H. et al.: Novel tools to improve patient selection and monitoring on active surveillance for low-risk prostate cancer: a systematic review. *Eur Urol*, **65**: 1023, 2014
4. Chamie, K., Sonn, G. A., Finley, D. S. et al.: The role of magnetic resonance imaging in delineating clinically significant prostate cancer. *Urology*, **83**: 369, 2014
5. Park, B. H., Jeon, H. G., Jeong, B. C. et al.: Influence of Magnetic Resonance Imaging in the Decision to Preserve or Resect Neurovascular Bundles at Robotic Assisted Laparoscopic Radical Prostatectomy. *J Urol*, 2014
6. Lee, D. J., Ahmed, H. U., Moore, C. M. et al.: Multiparametric magnetic resonance imaging in the management and diagnosis of prostate cancer: current applications and strategies. *Curr Urol Rep*, **15**: 390, 2014
7. Hambrock, T., Somford, D. M., Huisman, H. J. et al.: Relationship between apparent diffusion coefficients at 3.0-T MR imaging and Gleason grade in peripheral zone prostate cancer. *Radiology*, **259**: 453, 2011
8. White, N. S., McDonald, C. R., Farid, N. et al.: Improved conspicuity and delineation of high-grade primary and metastatic brain tumors using "restriction spectrum imaging": quantitative comparison with high B-value DWI and ADC. *AJNR Am J Neuroradiol*, **34**: 958, 2013
9. White, N. S., Leergaard, T. B., D'Arceuil, H. et al.: Probing tissue microstructure with restriction spectrum imaging: Histological and theoretical validation. *Hum Brain Mapp*, **34**: 327, 2013
10. Donati, O. F., Afaq, A., Vargas, H. A. et al.: Prostate MRI: evaluating tumor volume and apparent diffusion coefficient as surrogate biomarkers for predicting tumor Gleason score. *Clin Cancer Res*, **20**: 3705, 2014
11. Kobus, T., Vos, P. C., Hambrock, T. et al.: Prostate cancer aggressiveness: in vivo assessment of MR spectroscopy and diffusion-weighted imaging at 3 T. *Radiology*, **265**: 457, 2012
12. Oto, A., Yang, C., Kayhan, A. et al.: Diffusion-weighted and dynamic contrast-enhanced MRI of prostate cancer: correlation of quantitative MR

- parameters with Gleason score and tumor angiogenesis. *AJR Am J Roentgenol*, **197**: 1382, 2011
13. Turkbey, B., Shah, V. P., Pang, Y. et al.: Is apparent diffusion coefficient associated with clinical risk scores for prostate cancers that are visible on 3-T MR images? *Radiology*, **258**: 488, 2011
 14. Vargas, H. A., Akin, O., Franiel, T. et al.: Diffusion-weighted endorectal MR imaging at 3 T for prostate cancer: tumor detection and assessment of aggressiveness. *Radiology*, **259**: 775, 2011
 15. Vargas, H. A., Donati, O. F., Wibmer, A. et al.: Association Between Penile Dynamic Contrast-Enhanced MRI-Derived Quantitative Parameters and Self-Reported Sexual Function in Patients with Newly Diagnosed Prostate Cancer. *J Sex Med*, 2014
 16. Donati, O. F., Mazaheri, Y., Afaq, A. et al.: Prostate cancer aggressiveness: assessment with whole-lesion histogram analysis of the apparent diffusion coefficient. *Radiology*, **271**: 143, 2014
 17. Holland, D., Kuperman, J. M., Dale, A. M.: Efficient correction of inhomogeneous static magnetic field-induced distortion in Echo Planar Imaging. *Neuroimage*, **50**: 175, 2010
 18. Peng, Y., Jiang, Y., Antic, T. et al.: Validation of quantitative analysis of multiparametric prostate MR images for prostate cancer detection and aggressiveness assessment: a cross-imager study. *Radiology*, **271**: 461, 2014
 19. Rosenkrantz, A. B., Triolo, M. J., Melamed, J. et al.: Whole-lesion apparent diffusion coefficient metrics as a marker of percentage Gleason 4 component within Gleason 7 prostate cancer at radical prostatectomy. *J Magn Reson Imaging*, 2014
 20. Tollefson, M. K., Leibovich, B. C., Slezak, J. M. et al.: Long-term prognostic significance of primary Gleason pattern in patients with Gleason score 7 prostate cancer: impact on prostate cancer specific survival. *J Urol*, **175**: 547, 2006
 21. Allaf, M. E., Partin, A. W., Carter, H. B.: The importance of pelvic lymph node dissection in men with clinically localized prostate cancer. *Rev Urol*, **8**: 112, 2006
 22. Klotz, L., Zhang, L., Lam, A. et al.: Clinical results of long-term follow-up of a large, active surveillance cohort with localized prostate cancer. *J Clin Oncol*, **28**: 126, 2010

Tables

Table 1: MRI scan parameters for prostate MRI protocol at 3T.

Table 2: Demographics: Perioperative demographics for 28 patients who underwent MRI with an endorectal coil and subsequently underwent radical prostatectomy.

Table 3: Univariable analysis: Restriction spectrum imaging (RSI) z-score and apparent diffusion coefficient (ADC) are independently investigated comparing individual regions of interest to their corresponding primary Gleason pattern. The top half of the table uses ANVOA analysis to determine differences in detection comparing benign vs. primary Gleason 3 vs. Primary Gleason 4 prostate cancer. The bottom half of the table only compares Gleason 3 vs. 4 cancers with a t-test.

Table 4: Multivariable analysis: Restriction spectrum imaging (RSI) z-score and apparent diffusion coefficient (ADC) are independently investigated comparing individual regions of interest to their corresponding primary Gleason pattern. The top half of the table uses ordinal logistic regression analysis to determine differences in detection comparing benign vs. primary Gleason 3 vs. Primary Gleason 4 prostate cancer (Log Odds). The bottom half of the table only compares Gleason 3 vs. 4 cancers to determine with binary logistic regression (Odds Ratio).

Figures

Figure 1: Representative images showing RSI z-score maps across Gleason scores: The y-axis shows the pathologic Gleason score with the x-axis designating the MRI sequence. The last column displays the whole mount pathology with the corresponding cancer region of interest circled in black. The star in the top right pathologic figure represents the pattern 3+3 prostate cancer while the other lesions are 4+3. White arrowheads in the higher grade patients show areas of signal void which could be interpreted as false positives on the ADC maps.

Figure 2: RSI-z Score Value Grouped by Pathologic Gleason Score: The y –axis represents the RSI z-score derived from a given region of interest. The x-axis demonstrates the pathological Gleason scores in increasing levels of aggressiveness from left to right. Each data point represents one region of interest corresponding to a location on the whole mount prostatectomy specimen contoured by a GU pathologist.

Figure 3: Box Plot of RSI z-Score for Primary Gleason Pattern: The box-plot represents the RSI z-Score for benign, pathologic primary pattern Gleason 3, or pathologic primary pattern Gleason 4 prostate cancer.

Table 1

MRI scan parameters for prostate MRI protocol at 3T	
Pulse sequence	Parameters
T2	Axial 3D TSE T2 (Siemens SPACE, TR/TE 3800-5040/101 ETL 13, 14 cm FOV, 256 x 256 matrix, 1.5 mm contiguous slices)
Diffusion-weighted (Standard)	(echoplanar, TR/TE 3900/60, 21 x 26 cm FOV, 130 x 160 matrix, 3.6 mm slices, 4 NEX, b-values 0, 100, 400, 800 s/mm ²)
T1 Dynamic Perfusion Imaging	(Siemens TWIST, TR./TE 3.9/1.4 ms, 12° flip angle, 26 x 26 cm FOV, 160 x 160 matrix, 3.6 mm slices, 4.75 s/acquisition over 6 minutes with 15 s injection delay, image analysis using iCAD Versavue)
Restriction Spectrum Imaging	Spin echo EPI, TR/TE 5500/137, 26 x 26 cm FOV, 128 x 96 matrix, 3.6 mm slices, 30 directions at each b-value, b-values 0, 800, 1500, 4000 s/mm ² .

Table 2

ID	Age	Race	Body Mass Index	Preoperative PSA	Biopsy Gleason	Prostatectomy Gleason	Pathologic Stage	PIRADS Score
1	63	White	20.1	7	3+4	3+3	pT2	4
2	53	Asian	16.9	5.5	3+4	3+4	pT2 Nx Mx	4
3	58	White	32.7	3.8	3+4	3+4	pT2c Nx Mx	3
4	44	White	26.6	2.8	3+4	3+4	pT2a N0 Mx	3
5	53	White	22.7	3.9	4+3	3+4	pT3a pN0 Mx	2
6	50	White	31.2	8.9	3+4	3+4	pT2 Nx Mx	4
7	65	Unknown	29	5.4	3+4	3+4	pT2 Nx Mx	2
8	61	White	29.8	6.6	4+3	3+4	pT2 N0 Mx	4
9	60	-	25.5	6	3+3	3+4	pT2 pNx Mx	3
10	61	Other	26	3.4	3+4	3+4	pT2c N0 Mx	3
11	64	White	23.1	5.8	3+4	3+4	pT2c Nx Mx	2
12	55	White	27.5	4.7	3+4	3+4	pT2b N0 Mx	3
13	68	White	-	6.7	3+4	3+4	pT2c N0 Mx	3
14	61	White	21.4	9.2	3+3	3+4	pT2 N0 Mx	4
15	59	White	31.4	4.43	3+3	3+4	pT2c Nx Mx	3
16	71	White	29.7	7.3	3+3	3+4	pT2	3
17	55	White	29.3	2.8	3+5	3+4	pT3a	3
18	61	White	31.4	5.8	4+3	3+4	pT3b	5
19	71	White	28.4	12.8	4+3	4+3	pT3a pN1 Mx	5
20	67	White	30.4	5.1	3+4	4+3	pT3a pN0 Mx	4
21	56	Other	28	-	3+4	4+3	pT3a N0 Mx	4
22	64	White	26.9	4.2	3+5	4+3	pT3a	5
23	65	White	38.5	5.8	4+3	4+3	pT3a	5
24	62	Black	25.1	4.8	4+3	4+3	pT2a N0 Mx	0
25	45	Black	23.5	6.5	4+3	4+4	pT2c N0 Mx	1
26	70	Filipino	35.5	7.5	3+4	4+5	pT3a pNx Mx	3
27	62	White	25.8	4.6	4+5	4+5	pT2 N0 Mx	4
28	65	White	30.1	8.2	5+4	4+5	pT3b	4

Table 3

Sample Size	Method		Means	Statistical Test	P Value
Detection of Increasingly Aggressive Cancer*			Mean (Standard Error)	F test	
64	Restricted Spectrum Imaging (RSI) z-score			97.7	<0.001
		Benign	0.65 (0.12)		
		Primary			
		Gleason 3	2.4 (0.61)		
		Primary			
		Gleason 4	2.9 (0.51)		
64	Apparent Diffusion Coefficient (ADC)			13.9	<0.001
		Benign	1680 (428)		
		Primary			
		Gleason 3	1237 (425)		
		Primary			
		Gleason 4	967 (221)		
Prostate Cancer Aggressiveness**			Mean Difference	t test	
36	Restricted Spectrum Imaging (RSI) z-score	34	0.5	2.22	0.033
36	Apparent Diffusion Coefficient (ADC)	34	269	1.81	0.079

Table 4

Sample Size	Method		Parameter Coefficient ^a (95% Confidence Interval)	P Value	McFadden's D
<i>Detection of Increasingly Aggressive Prostate Cancer^b</i>					
64	Restricted Spectrum Imaging (RSI) z-score			<0.001	0.613
		Benign	0		
		Primary Gleason 3	9.5 (-1.9 - 17.0)	0.014	
		Primary Gleason 4	15.8 (6.4 - 25.2)	0.001	
64	Apparent Diffusion Coefficient (ADC)			<0.001	0.202
		Benign	0		
		Primary Gleason 3	1.7 (-3.2 - 6.7)	0.483	
		Primary Gleason 4	4.5 (-0.5 - 9.6)	0.076	
<i>Prostate Cancer Aggressiveness^c</i>		Wald test	Odds Ratio (95% Confidence Interval)	P Value	
36	Restricted Spectrum Imaging (RSI) z-score	5.1	10.3 (1.4-78.0)	0.024	
36	Apparent Diffusion Coefficient (ADC)	3.3	0.9 (0.9-1.00)	0.069	

Figure 1

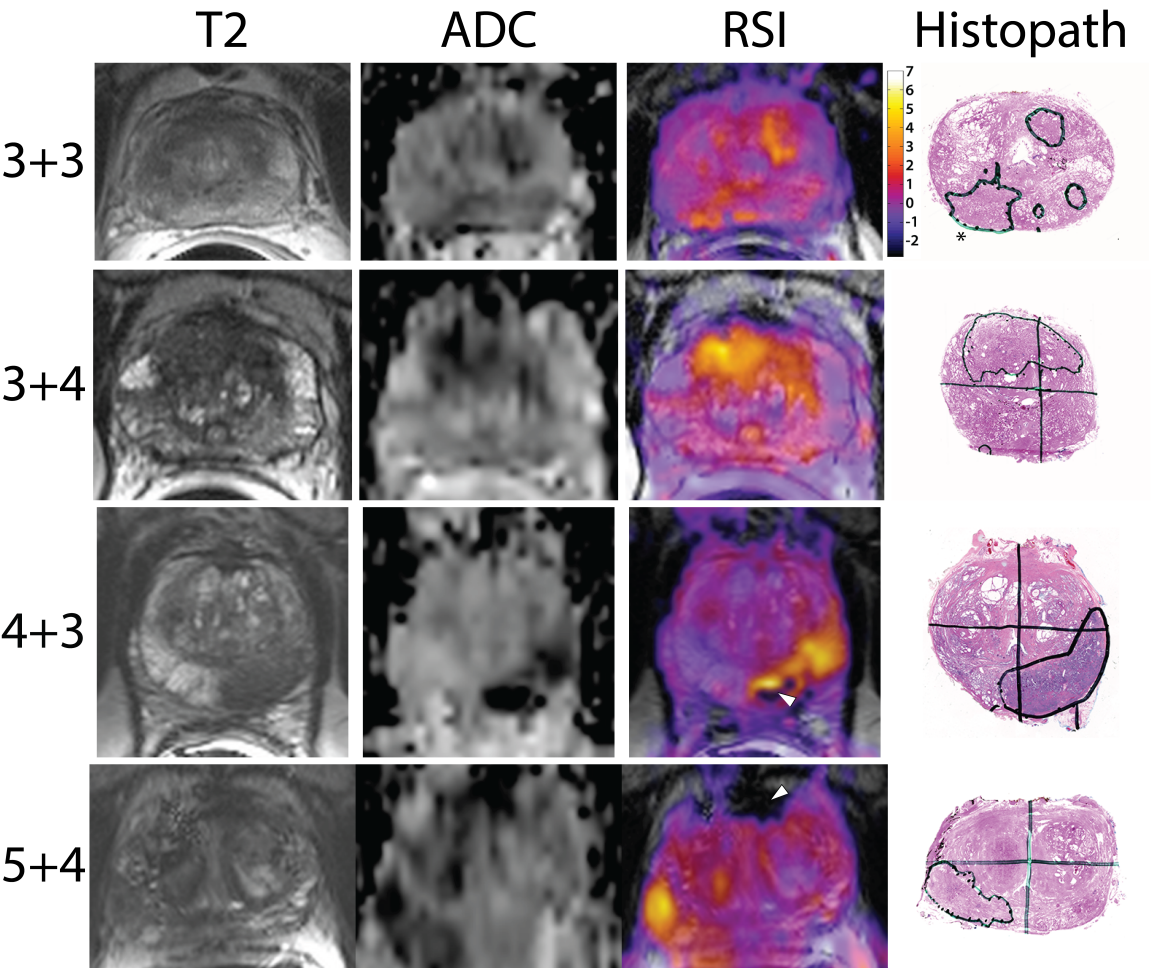


Figure 2

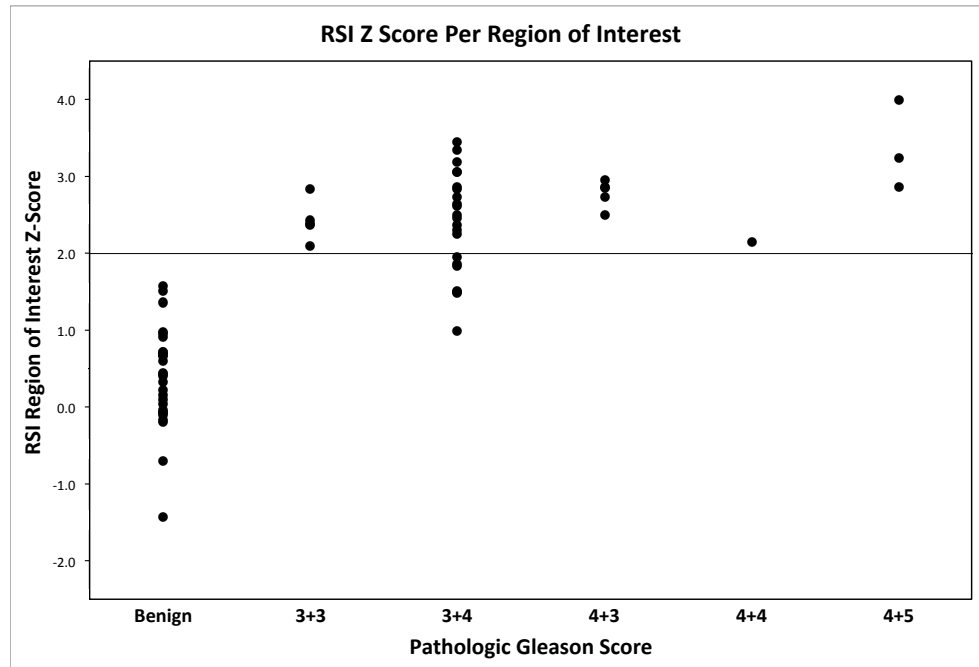
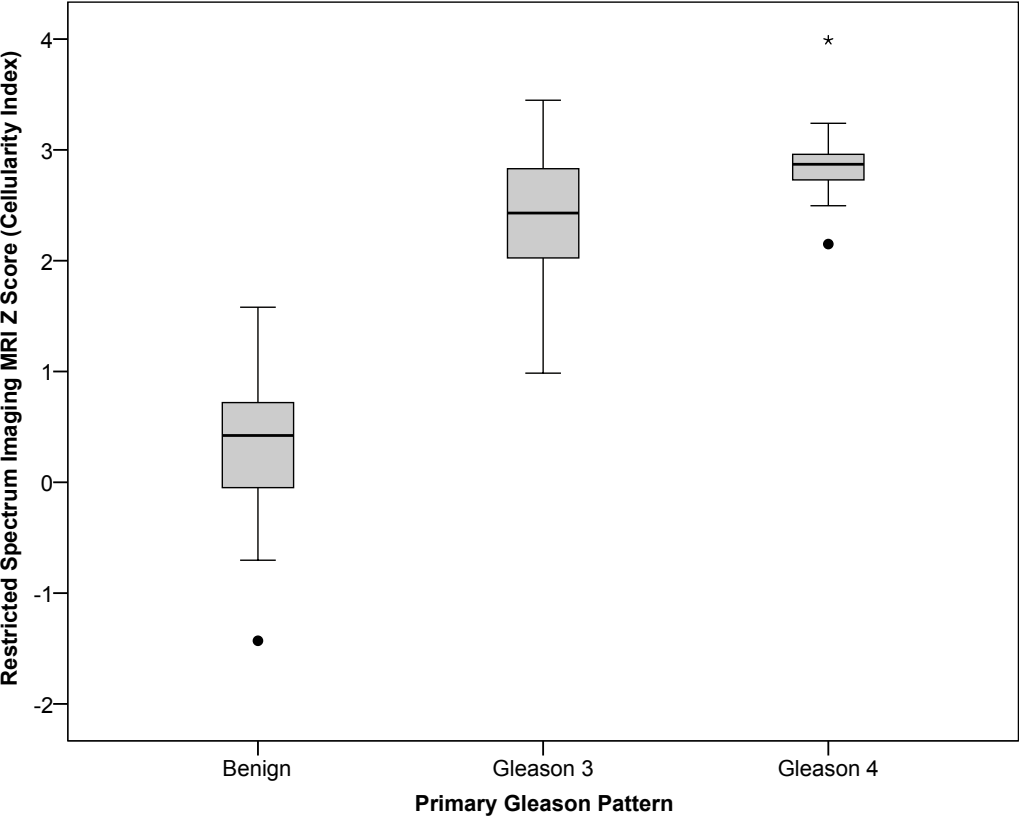


Figure 3



EXTRA FIGURE: CORRELATION

